J. Fluid Mech. (2007), *vol.* 578, *pp.* 171–222.
doi:10.1017/S0022112007004934 Printed in the United Kingdom

Analysis of cavitating flow structure by experimental and numerical investigations

O. COUTIER-DELGOSHA[1]†, B. STUTZ[2], A. VABRE[3] AND S. LEGOUPIL[3]

[1]ENSTA - UER de Mécanique, Chemin de la Hunière, 91761 Palaiseau Cedex, France
[2]CETHYL, 20 Avenue Albert Einstein, 69621 Villeurbanne-cedex, France
[3]Commissariat à l'Energie Atomique (CEA), CEA-Saclay, DRT/LIST, 91191 Gif sur Yvette, France

(Received 28 March 2006 and in revised form 2 November 2006)

The unsteady structure of cavitating flows is investigated by coupled experimental and numerical means. Experiments focus on the structure and dynamics of sheet cavitation on the upper side of a two-dimensional foil section in the ENSTA cavitation tunnel. Various flow conditions are investigated by varying the pressure, the flow velocity, and the incidence of the foil section. High-frequency local measurements of volume fractions of the vapour phase are performed inside the liquid/vapour mixture by a X-ray absorption method. The numerical approach is based on a macroscopic formulation of the balance equations for a two-phase flow. The assumptions required by this formulation are detailed and they are shown to be common to almost all the models used to simulate cavitating flows. In the present case we apply a single-fluid model associated with a barotropic state law that governs the mixture density evolution. Numerical simulations are performed at the experimental conditions and the results are compared to the experimental data. A reliable agreement is obtained for the internal structure of the cavity for incidence varying between 3° and 6°. Special attention is paid to the mechanisms of partial and transitional instabilities, and to the effects of the interaction between the two sides of the foil section.

1. Introduction

Turbopumps of rocket cryogenic engines operate in cavitating conditions because of the low pressure in hydrogen and oxygen tanks. Therefore, the first stage of these pumps usually consists of an axial runner called an inducer, in which the incoming flow vaporizes on the blade suction side and in the other low-pressure areas, located mainly at the tip. At the outlet, the pressure of the fluid is high enough to avoid any risk of cavitation in the subsequent centrifugal stages of the pump. The design of the inducer is of prime importance, since its performance must be maintained even in cavitating conditions. The presence of vapour in the inducer modifies the blade load, which can rapidly lead to a diminution of performance.

Moreover, cavitation is responsible for several instabilities that affect the global behaviour of the pump. The first one consists of a coupling between the blade-to-blade channels, leading to non-symmetrical structures of vapour in the inducer. These flow patterns cause some important forces on the inducer casing and on

† Present address: ENSAM Lille/LML laboratory, 8 boulevard Louis XIV, 59046 Lille cedex, France.

the other pump components. They have been reported by Kamijo, Shimura & Watanabe (1977) and de Bernardi, Joussellin & Von Kaenel (1993), and modelled numerically by Tsujimoto, Kamijo & Yoshida (1993) and Coutier-Delgosha *et al.* (2004). The second flow instability consists of the self-oscillatory behaviour of each sheet of cavitation, occurring mainly at the partial flow rate, which can result in severe pressure fluctuations at the inducer outlet. This phenomenon has been studied experimentally in cavitation tunnels by many authors (Kubota, Kato & Yamaguchi 1992; Chen & Heister 1996; Stutz & Reboud, 1997*a*, 2000; Kjeldsen, Arndt & Efferts 2000; Leroux, Coutier-Delgosha & Astolfi 2005) to understand the mechanisms of the fluctuations. Venturi-type sections and two-dimensional foil sections have both been used to obtain unsteady sheet cavitation and to investigate its behaviour. These studies have considerably improved the understanding of the cavity dynamics: the occurrence of a re-entrant jet under the cavity, that flows upstream and results periodically in cavity break off, was demonstrated for example by Stutz & Reboud (1997*b*) with double optical probe measurements and by Pham, Larrarte & Fruman (1999) with electrical impedance probes. This process, initially described by Furness & Hutton (1975), results in the periodical detachment of the rear part of the cavity, and its convection downstream until it collapses. Other reasons for the flow unsteadiness, such as a combination of a re-entrant jet with a periodic interface destabilization in the downstream end of the cavity, were proposed by Lush & Peters (1982). More recently, the pressure wave resulting from the cloud collapse has been investigated by Leroux *et al.* (2005), both experimentally and numerically. The magnitude of this wave has been found to influence significantly the frequency of the periodical cavitation cycle.

However, up to the present time, only a few authors have investigated the internal structure of such cavitating flow, whether by experimental means (Stutz & Reboud 1997*a*,*b*, 2000; Gopalan & Katz 2000) or by numerical calculations (Reboud, Stutz & Coutier 1998; Coutier-Delgosha, Reboud & Delannoy 2003*a*). This aspect is essential for improving understanding of the mechanisms governing vapour creation and cavity fluctuations. But most of the studies have focused on the external liquid flow (Ceccio & Brennen 1992, Le, Franc & Michel 1993) with no information about the two-phase flow inside the vaporized areas. This is mainly due to the difficulties involved in such investigations: the volume fraction of the vapour phase varies in the range 0 to 1, with bubbles of various sizes, from a few μm to a few mm, affected not only by the periodic vapour cloud shedding but also by high-frequency fluctuations. More recently a double optical probe device has been developed by Stutz & Reboud (1997*a*, *b*) and applied to the measurement of both the velocity and the void fraction within steady and unsteady sheet cavities in a Venturi-type section. This work confirmed the presence of the re-entrant jet, and also provided some first indications concerning the two-phase structure: the void ratio was found to not exceed 50 % in the case of steady sheet cavitation, and 25 % in the case of unsteady cavities. However, the uncertainty on the measurements was estimated as about 15 % by the authors. Global measurements of the volume fraction of vapour within the cavity in the same flow configuration also performed by Stutz & Legoupil (2003) with a X-ray attenuation device. The results corroborated the optical probe measurements. However, the aim of that work was not to determine local information about the flow inside the sheet cavity.

The present paper is devoted to the study of the unsteady two-phase flow structure of sheet cavitation by a coupled experimental/numerical approach. The configuration consists of a two-dimensional foil section positioned at a low incidence in a cavitation tunnel. The flow velocity is varied from $U_{ref} = 5\,\mathrm{m\,s^{-1}}$ up to $9\,\mathrm{m\,s^{-1}}$, while the pressure

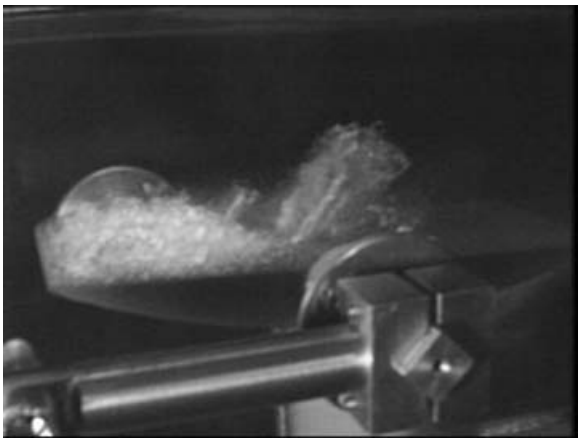

FIGURE 1. Sheet cavitation on the upper face of the two-dimensional foil section.

is adjusted to obtain cavitation numbers $\sigma = (P\text{-}P_v)/\frac{1}{2}\rho_l U_{ref}^2$ varying between 0.6 and 1.4, where P_v denotes the vapour pressure, U_{ref} the flow velocity at the inlet of the test section, and ρ_l the liquid density. Sheet cavitation is obtained on the upper side of the foil, as shown in figure 1. Its length and behaviour depend on the flow conditions. Three values of the foil angle of attack are considered (3°6′, 4°42′, 5°54′) in order to obtain a range of unsteady behaviour. An X-ray attenuation device is used to measure locally the instantaneous value of the volume fraction $\beta = V_v/V$, with V a measurement volume and V_v the vapour volume inside. Unlike the previous experiments of Stutz & Legoupil, the measurement volumes here are discretized not only in the flow direction but also along the cavity height, in order to obtain the evolution of the volume fraction of vapour from the foil surface up to the limit of the vaporized area. Fast data acquisition (1000 Hz) enables the measurement of the time/space distribution of the vapour phase during the vapour shedding cycles. Moreover, the whole cavitating area is investigated, from the foil leading edge to the cavity far wake, in order to calculate unsteady flow characteristics such as the convection velocity of the vapour clouds.

Numerical simulations of cavitating flows are usually based on a coupling between the resolution of the Reynolds-averaged Navier–Stokes (RANS) equations and a physical model of cavitation. For some of these models, only the influence of the sheet cavity on the external liquid flow has been considered (Dang & Kuiper 1998; Kai & Ikehata 1998). Therefore only the outer flow was calculated, and almost no information is available concerning the internal liquid/vapour structure. This kind of method only applies in the particular configuration of stable sheet cavitation, and peripheral cavitating secondary flows in inducers cannot be simulated with this approach. Unsteady behaviours and the vapour cloud shedding involved in cavity self-oscillations are also usually outside the scope of these models.

To treat unsteady phenomena, the RANS equations are usually solved in the whole computational domain, including the cavitating areas (Delannoy & Kueny 1990; Chen & Heister 1994; Grogger & Alajbegovic 1998; Kunz *et al.* 2000; Coutier-Delgosha *et al.* 2003*a*). In these models, the behaviour of the liquid/vapour mixture has been calculated using several different methods: some authors have proposed a state law for the mixture (Delannoy 1989; Song & He 1998), while others consider the evolution of bubbles on the basis of the Rayleigh–Plesset equation (Kubota *et al.*

1992; Singhal *et al.* 2002) or express the mass transfers between liquid and vapour in terms of the local inequality between the pressure and the vapour pressure (Reboud & Stutz 1995; Merkle, Feng & Buelow 1998; Kunz *et al.* 2000; Senocak & Shyy 2004*a*). In the last ten years, volume-of-fluid (VOF) methods based on interface tracking (Dieval, Arnaud & Marcer 1998) have also been efficiently applied.

In the present case we apply a single-fluid model: this means that the vapour/liquid medium is considered as a homogeneous fluid the density of which is governed by a barotropic-state law initially proposed by Delannoy & Kueny (1990). To make clear the equations solved in this model and the assumptions that are involved, § 2 focuses on the balance equations for a cavitating flow and the successive simplifications that are required. The objective is to find how the balance equations that are commonly considered in a cavitation problem are obtained, and to determine what physical assumptions are applied in the usual cavitation models.

Sections 3 and 4 are devoted to the presentation of the experimental device and the numerical model, respectively. Calculations are carried out at the experimental flow conditions. In § 5, the two-phase flow structure is investigated, on the basis of the experiments. The numerical results are also compared to the experimental data to demonstrate the capability of the model to simulate both the general behaviour of the sheet cavities and their local structure. Then, a more detailed analysis is performed in § 6 to understand the process of vapour creation and convection inside the cavity.

2. Physical model of cavitation

This section is devoted to the presentation of the physical model that is applied to treat the vaporization and condensation processes and the interactions between liquid and vapour. Special attention is paid to the significance of the equations that are used and also to the assumptions that they involve. The objective is to compare the different models usually applied and also to justify the physical approach that is used to obtain the numerical results in the present work.

In most of the models applied to numerical simulations of cavitating flows, the mass balance equation is expressed in two ways: either for each of the two phases, according to

$$\begin{aligned} &\frac{\partial(\beta_k \rho_k)}{\partial t} + \nabla \cdot (\beta_k \rho_k \boldsymbol{U}_k) = \Gamma_k, \\ &\sum \Gamma_k = 0 \end{aligned} \tag{2.1}$$

where $\boldsymbol{U}_k$ is a velocity characterizing phase k (its definition will be discussed hereafter), and Γ_k is the interfacial mass source in phase k due to vaporization or condensation; or for the medium composed of the two phases, with a supplementary diffusion equation for one of the two phases

$$\frac{\partial(\rho_m)}{\partial t} + \nabla \cdot (\rho_m \boldsymbol{U}_m) = 0, \tag{2.2}$$

$$\frac{\partial(\beta_v \rho_v)}{\partial t} + \nabla \cdot (\beta_v \rho_v \boldsymbol{U}_m) = \Gamma_v, \tag{2.3}$$

where indices m and v refer respectively to the mixture and to the vapour phase. The momentum balance equation,

$$\frac{\partial(\rho_m \boldsymbol{U}_m)}{\partial t} + \nabla \cdot (\rho_m \boldsymbol{U}_m \cdot \boldsymbol{U}_m) = \nabla \cdot \Pi_m, \tag{2.4}$$

is written systematically for the medium, so the slip between the two phases is not considered. All these equations involve a parameter $\beta_k (k = v, l)$ that denotes the local volume fraction of phase k: its usual definition in the numerical simulations is $\beta_k = V_k / V$ where V denotes the volume of each cell and V_k the proportion of this volume occupied by phase k. In the papers devoted to the simulation of cavitating flows, β_v is systematically denoted α_v or α, and called the void fraction. However, neither the notation nor the appellation are appropriate, since in the two-phase flow community the void fraction $\alpha(M)$ commonly equals $\Delta t_k / \Delta t$, where Δt_k is the time of presence of phase k at point M during the time Δt.

In the present paper, the notations β_v or β are used for the volume fraction of the vapour phase.

Equations (2.1)–(2.4) appear to be derived from the ones proposed initially by Ishii (1975), who obtained averaged formulations: in the first, the two phases are considered separately, with interaction terms between them (two-fluid model), while in the second only one set of equations is applied for the medium composed of the two phases (diffusion model). However, Ishii obtains these equations by time-averaging the local instant formulation equations over a period Δt, which is "large enough to smooth the local variations of properties", but small compared to the scale of the macroscopic flow unsteadiness. So in this case, the equations involve the local void fraction α_k, instead of the volume fraction β_k. However, as was mentioned previously, in the literature devoted to the simulation of cavitation and in the community, β_k is systematically denoted the "void fraction α", which makes equations (2.1) to (2.4) apparently identical to the ones obtained by Ishii. So, most of the time, the above equations are applied to cavitation without any further discussion.

Conversely, some authors indicate that they were obtained by density-weighted averaging of the local instant formulation equations (Thai Van *et al.* 1994), while others refer to the work of Drew (1983). Drew revisited the features of two-phase flows and proposed a general formulation of the equations for the different types of averaging. In the particular case of space averaging, the above equations are obtained with the appropriate definition of β_k. However, the physical meaning of the velocities $\boldsymbol{U}_k$ and $\boldsymbol{U}_m$ is not straightforward. $\boldsymbol{U}_k$ is defined by the following relation:

$$\boldsymbol{U}_k = \langle \chi_k \rho \boldsymbol{u} \rangle / \beta_k \tilde{\rho}_k \tag{2.5}$$

where $\langle\ \rangle$ denotes the averaging process, $\boldsymbol{u}$ is the local velocity, ρ the local density, and χ_k is the phase density function defined to be:

$$\chi_k(\mathrm{M}, \mathrm{t}) = \begin{cases} 1 & \text{if M is in phase } k \text{ at time } t \\ 0 & \text{otherwise} \end{cases} \tag{2.6}$$

and

$$\tilde{\rho}_k = \langle \chi_k \rho \rangle / \beta_k. \tag{2.7}$$

In the same way, $\boldsymbol{U}_k \cdot \boldsymbol{U}_k$ refers to $\langle \chi_k \rho \boldsymbol{u} \cdot \boldsymbol{u} \rangle / \beta_k \tilde{\rho}_k$, and not to $\langle \chi_k \rho \boldsymbol{u} \rangle / \beta_k \tilde{\rho}_k \times \langle \chi_k \rho \boldsymbol{u} \rangle / \beta_k \tilde{\rho}_k$.

So $\boldsymbol{U}_k$ and $\boldsymbol{U}_k \cdot \boldsymbol{U}_k$ result from mathematical definitions but theoretically they may not be directly connected to each other. The same discrepancy occurs for the mixture velocity $\boldsymbol{U}_m = \sum (\rho_k \boldsymbol{U}_k / \rho_m)$, where $\rho_m = \sum \beta_k \rho_k$. The physical significance of velocities $\boldsymbol{U}_k$ and $\boldsymbol{U}_m$ is thus difficult to handle. The definition of β_k also brings some confusion: although equations (2.1) to (2.4) are usually called *local* balance equations for the two phases and/or the medium, β_k is a volume fraction defined in a control volume V whose size should be properly defined. This inconsistency usually vanishes

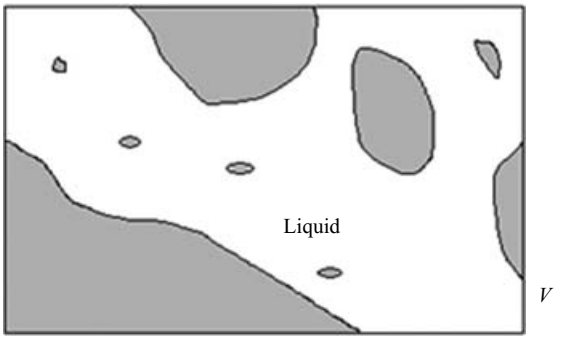

FIGURE 2. Illustration of the control volume V.

when the equations are discretized, since V is then identified with the volume of the cells. However, the formulation of the equations in the physical models should be clarified.

In the present work we derive the equations (2.1) to (2.4) from the mass and momentum balance in a control volume V. No averaging is performed, but a condition is given on the size of the control volume, in order to define some macroscopic variables at the scale of V.

2.1. *Mass balance equations for a two-phase flow*

We consider in this section a volume V of fluid in a liquid/vapour mixture. Its geometric contour is assumed stationary and it is continuously crossed by the flow. So, V contains a vapour/liquid mixture that fluctuates in time. Thus, the vapour and the liquid volumes in V, namely V_v and V_l, also fluctuate. The boundary of V is denoted S, and ρ_v, ρ_l refer respectively to the vapour and liquid densities, which are both assumed to be constant. Figure 2 is a schematic illustration of a possible composition of V at a given time. Note that the size of V will be discussed further hereafter, as it will appear to be a critical parameter of the problem, to obtain the classical equations applied to model cavitating flows.

The mass conservation in the volume V can be written as follows:

$$\frac{\partial}{\partial t}(\text{mass of vapour inside } V) = \text{mass fluxes across } S + \text{vaporization/condensation inside } V,$$

which can be expressed in an integral mathematic form:

$$\frac{\partial}{\partial t}\left[\iiint_V \chi_v \rho_v \, \mathrm{d}\tau\right] = -\oiint_S \chi_v \rho_v (\boldsymbol{u}_v \cdot \boldsymbol{n}) \, \mathrm{d}s + \Gamma_v V \tag{2.8}$$

where $\boldsymbol{u}_v$ is the local velocity of the vapour inside V. The definition of χ_v according to equation (2.6) implies that only two states of the fluid (liquid and vapour) should be taken into account in V. This means that V is assumed to be much larger than the characteristic thickness of the interfaces between the two phases, so that this intermediate state of the fluid can here be neglected. The right-hand-side term $\Gamma_v V$ denotes the mass source term corresponding to the appearance or vanishing of vapour due to vaporization/condensation phenomena inside V.

The density ρ_v of vapour being constant, equation (2.8) becomes:

$$\frac{\partial}{\partial t}(\rho_v V_v) = -\rho_v \oiint_S (\chi_v \boldsymbol{u}_v \cdot \boldsymbol{n})\,\mathrm{d}s + \Gamma_v V = -\rho_v \iiint_V \nabla(\chi_v \boldsymbol{u}_v)\,\mathrm{d}\tau + \Gamma_v V \tag{2.9}$$

$$= -\rho_v \left[\iiint_V (\chi_v \nabla \boldsymbol{u}_v + \boldsymbol{u}_v \cdot \nabla \chi_v)\,\mathrm{d}\tau \right] + \Gamma_v V. \tag{2.10}$$

As mentioned previously, studies of cavitating flow usually focus on a macroscopic point of view: it implies that the precise motions of the very small bubbles inside V are unknown. They are only taken into account at the V scale by defining a constant macroscopic velocity $\boldsymbol{U}_v$ for the vapour inside V. Note that $\boldsymbol{U}_v$ does not result from any mathematical averaging, but only from the assumption that all bubbles have the same velocity inside the control volume. This implies that the volume V should be much smaller than the characteristic scale of the flow dynamics. A second condition on the size of V is thus obtained. This suggests an analogy with the notion of a fluid particle defined in single-phase conditions (volume of fluid much larger than the molecular scale and much smaller than the characteristic scale of the flow variations). We may define physically here a 'two-phase fluid particle' whose volume V is much larger than the thickness of the liquid/vapour interfaces, but also much smaller than the characteristic scales of the flow. All macroscopic variables, such as $\boldsymbol{U}_v$ and $\nabla \boldsymbol{U}_v$ can then be considered as constant inside the volume V. Note that the condition on the size of V is not much more restrictive than that on the size of a fluid particle, since the liquid/vapour interface thickness is about 1 nm (Caupin 2005), which represents only three molecular diameters.

Using the fact that volume V is stationary, equation (2.10) can thus be expressed in the form:

$$\rho_v \frac{\partial}{\partial t}(V_v) = -\rho_v \nabla \boldsymbol{U}_v \iiint_V \chi_v\,\mathrm{d}\tau - \rho_v \boldsymbol{U}_v \cdot \nabla \iiint_V \chi_v\,\mathrm{d}\tau + \Gamma_v V. \tag{2.11}$$

The definitions of χ_v and the volume fraction of vapour β lead to:

$$\iiint_V \chi_v\,\mathrm{d}z = V_v = \beta V. \tag{2.12}$$

The combination of relations (2.11) and (2.12) leads to

$$\rho_v \frac{\partial}{\partial t}(\beta V) = -\rho_v V \nabla \boldsymbol{U}_v \beta - \rho_v V \boldsymbol{U}_v \cdot \nabla \beta + \Gamma_v V. \tag{2.13}$$

Note that the initial equation, involving local values of the variables inside the integral signs, has been turned into a macroscopic relation, in which only the volume fraction of vapour β inside V and the macroscopic variables defined at V scale appear. Dividing by $\rho_v V$, the final expression for the mass conservation in V can be written

$$\frac{\partial \beta}{\partial t} + \nabla(\beta \boldsymbol{U}_v) = \frac{\Gamma_v}{\rho_v}. \tag{2.14}$$

This expression is the classical one used as the local mass equation for the vapour phase in a cavitating flow (Merkle *et al.* 1998; Reboud *et al.* 1998; Kunz *et al.* 2000). The same equation is obtained by considering a travelling volume V, and following the motion of the fluid particles that are initially contained inside. In this case, fluxes

across S are zero, but the corresponding terms are transferred in the Lagrangian time derivative.

The similar conservation of liquid inside V leads to the following analogous equation:

$$\frac{\partial(1-\beta)}{\partial t} + \nabla((1-\beta)\boldsymbol{U}_l) = -\frac{\Gamma_v}{\rho_l} \tag{2.15}$$

where $\boldsymbol{U}_l$ denotes the macroscopic velocity of the liquid inside V. The source term of the liquid inside V (corresponding to the fluid vaporization or condensation) is the opposite of the one that was used for the vapour: any vaporization during a time Δt of a liquid mass $m = \Gamma_v V \Delta t$, for example, induces a production of a vapour mass m as well as a vanishing of the same liquid mass.

2.2. *Momentum balance equations*

In the volume V, the momentum conservation for the vapour phase can be expressed as: $(\partial/\partial t)$ (Vapour momentum) = Momentum fluxes across S + Gradient of the external efforts acting on the vapour phase + Momentum exchanges inside V between vapour and liquid. It corresponds to:

$$\frac{\partial}{\partial t}\left[\iiint_V \chi_v \rho_v \boldsymbol{u}_v \,\mathrm{d}\tau\right] = -\oiint_S \delta \rho_v \boldsymbol{u}_v (\boldsymbol{u}_v \cdot \boldsymbol{n})\,\mathrm{d}s + \iiint_V \chi_v \nabla \pi_v \,\mathrm{d}\tau + \boldsymbol{M}_v V \tag{2.16}$$

where $\boldsymbol{M}_v V$ is the momentum transfer term from liquid to vapour, and π_v is the external stress tensor relative to the vapour phase. Note that the effect of gravity is neglected, which is a classical assumption for cavitating flows. The Froude number Fr based on the flow velocity U_{ref} and the vertical length scale L_v of the problem is usually much larger than one. In the experimental situation presented in § 3, L_v is the maximum thickness of the sheet cavity, i.e. about 3 cm, and $U_{ref} = 6\,\mathrm{m\,s^{-1}}$, so $Fr \sim 11$. This gives:

$$\frac{\partial}{\partial t}(\rho_v \boldsymbol{U}_v V_v) = -\rho_v \iiint_V \nabla\left(\chi_v \boldsymbol{u}_v^2\right) \mathrm{d}z + \iiint_V \chi_v \nabla \pi_v \,\mathrm{d}\tau + \boldsymbol{M}_v V \tag{2.17}$$

Recall that $\nabla(\boldsymbol{u}_v^2)$ is simply notation for a vector, the components of which are $c_i = \nabla[\rho_v (\boldsymbol{u}_v)_i \boldsymbol{u}_v]$. As previously, the condition on the size of the control volume V results in considering all macroscopic variables, such as $\boldsymbol{U}_v^2$, $\nabla(\boldsymbol{U}_v^2)$, and the external macroscopic stresses denoted Π_v, as constant inside V. Thus they can be moved outside the integral signs, as in the mass balance equations. This finally leads to:

$$\rho_v \frac{\partial}{\partial t}(\boldsymbol{U}_v V_v) = -\rho_v \nabla\left(\boldsymbol{U}_v^2\right) V_v - \rho_v \boldsymbol{U}_v^2 \nabla(V_v) + V_v \nabla D_v + \boldsymbol{M}_v V. \tag{2.18}$$

Then, introducing the volume fraction of vapour β and dividing by $\rho_v V$:

$$\frac{\partial}{\partial t}(\beta \boldsymbol{U}_v) = -\beta \nabla\left(\boldsymbol{U}_v^2\right) - \boldsymbol{U}_v^2 \nabla \beta + \frac{\beta}{\rho_v}\nabla \Pi_v + \frac{\boldsymbol{M}_v}{\rho_v}, \tag{2.19}$$

$$\frac{\partial}{\partial t}(\beta \boldsymbol{U}_v) + \nabla\left(\beta \boldsymbol{U}_v^2\right) = \frac{\beta}{\rho_v}\nabla \Pi_v + \frac{\boldsymbol{M}_v}{\rho_v}. \tag{2.20}$$

The corresponding momentum conservation can be obtained for the liquid phase:

$$\frac{\partial}{\partial t}((1-\beta)\boldsymbol{U}_l) + \nabla\left((1-\beta)\boldsymbol{U}_l^2\right) = \frac{1-\beta}{\rho_l}\nabla \Pi_l + \frac{\boldsymbol{M}_l}{\rho_l} \tag{2.21}$$

where $\boldsymbol{M}_l V$ is the momentum transfer term from vapour to liquid, which is *a priori* not equal to $-\boldsymbol{M}_v V$, when the surface tension σ_s is taken into account, and π_l is the external stress tensor relative to the liquid phase.

2.3. *Closure law*

The governing equations have been written for the liquid and vapour, resulting in two scalar equations and two vectorial ones. The system involves two vectorial unknowns $\boldsymbol{U}_v$, $\boldsymbol{U}_l$, and three scalar ones: the volume fraction of the vapour phase β and the pressures P_v, P_l in the vapour and the liquid phases (contained in the stress tensors Π_v and Π_l). A final scalar relation is thus missing for the system to be closed. It may consist of a local jump condition at the interface, relating P_v and P_l to the local interface curvature and to the surface tension σ_s. No macroscopic information is available concerning the shape and the position of each interface inside V, so the local curvature can only be derived from the bubble radius, assuming that all inclusions are spherical. However, the size of the vapour bubbles varies between a few μm and a few mm. Moreover, in the experiments performed in cavitation tunnels, vapour bubbles are nucleated from small air bubbles, so they contain some air that should be taken into account, since it modifies the internal pressure of the bubbles. The very small air-filled bubbles are characterized by a high surface tension, while the large ones are mainly composed of vapour, and their surface tension has much decreased. The transition between the two situations depends on a critical pressure value in the liquid, as explained by La Porta et al. (2000).

The presence of air is usually not considered in the cavitation models, so the effects of surface tension are systematically neglected, and liquid and vapour are assumed to be at the same pressure inside V: $P_v = P_l$. In the present experimental investigations, visualizations were performed inside the sheet cavity with an endoscopic device (Coutier-Delgosha et al. 2006), and it was estimated that most of the bubbles are larger than $R = 1$ mm. A rough estimation of $P_v - P_l$ with the Laplace law for such a bubble radius gives $P_v - P_l = 2\sigma_s/R = 145$ Pa, which is small compared with the scale of pressure variations during vaporization and condensation, i.e. 2700 Pa (see § 2.5). This confirms that the effects of surface tension can be neglected in a first approximation.

Therefore momentum fluxes are assumed to be identical from vapour to liquid and from liquid to vapour: $\boldsymbol{M}_l = -\boldsymbol{M}_v$.

Energy balance equations involving transfer terms between vapour and liquid can be also written for both phases. Moreover, turbulence also leads to a coupling between vapour and liquid. These mechanisms are usually neglected, so we focus hereafter on the different models that are applied to express the mass and momentum transfer terms Γ_k and $\boldsymbol{M}_k$.

2.4. *Single-fluid approach*

The two models proposed by Ishii (1975), namely the 'two-fluid model' and the 'diffusion model' are based on two different physical approaches, and also related to distinct systems of equations. The two-fluid model is derived from equations (2.14), (2.15), (2.20), and (2.21) for the two phases, whereas the diffusion model is based on the assumption that the liquid and the vapour have the same dynamics. In this case the slip between the two phases is neglected, and thus $\boldsymbol{U}_v = \boldsymbol{U}_l = \boldsymbol{U}_m$ and $\Pi_v = \Pi_l = \Pi_m$. The diffusion model focuses on the behaviour of the medium composed of both vapour and liquid. The equations can be derived from the previous ones, with the

definition for the medium density: $\rho_m = \beta\rho_v + (1-\beta)\rho_l$.

$$\frac{\partial(\rho_m)}{\partial t} + \nabla\cdot(\rho_m \boldsymbol{U}_m) = 0, \tag{2.22}$$

$$\frac{\partial\beta}{\partial \mathrm{t}} + \nabla(\beta \boldsymbol{U}_m) = \frac{\Gamma_v}{\rho_v} \tag{2.23}$$

(equations derived from the mass balance);

$$\frac{\partial}{\partial t}(\rho_m \boldsymbol{U}_m) + \nabla\left(\rho_m \boldsymbol{U}_m^2\right) = \nabla\Pi_m, \tag{2.24}$$

$$\frac{\partial}{\partial t}(\beta \boldsymbol{U}_m) + \nabla\left(\beta \boldsymbol{U}_m^2\right) = \frac{\beta}{\rho_v}\nabla\Pi_m + \frac{\boldsymbol{M}_v}{\rho_v} \tag{2.25}$$

(equations derived from the momentum balance).

The diffusion model is currently applied in most simulations of cavitation. It is usually denoted 'single-fluid model' (Delannoy & Kueny 1990; Chen & Heister 1994; Grogger & Alajbegovic 1998; Arndt *et al.* 2000; Coutier-Delgosha *et al.* 2003*a*) because the two phases are considered as a single fluid. Some authors refer to a 'two-fluid model' when they consider separate mass equations (2.14) and (2.15) for liquid and vapour (Merkle *et al.* 1998; Kunz *et al.* 2000). However, in these works no slip is considered between liquid and vapour, and only one momentum equation is solved for the medium, so basically all these models are based on the diffusion model initially proposed by Ishii.

In the diffusion model only equation (2.24) is considered for the momentum balance, while equation (2.25) is not solved. This suggests that equation (2.25) is implicitly assumed to be redundant when used with equation (2.24). However, this is true only for a particular expression for the momentum fluxes $\boldsymbol{M}_v$.

Equation (2.25) can be expressed in the form

$$\rho_v\beta\frac{\partial \boldsymbol{U}_m}{\partial t} + \rho_v \boldsymbol{U}_m\frac{\partial\beta}{\partial t} + \rho_v\beta \boldsymbol{U}_m\nabla(\boldsymbol{U}_m) + \rho_v \boldsymbol{U}_m\nabla(\beta \boldsymbol{U}_m) = \beta\nabla\Pi_m + \boldsymbol{M}_v. \tag{2.26}$$

The different terms can be grouped according to the following expression:

$$\rho_v \boldsymbol{U}_m\left[\frac{\partial\beta}{\partial t} + \nabla(\beta \boldsymbol{U}_m)\right] + \rho_v\beta\left[\frac{\partial \boldsymbol{U}_m}{\partial t} + \boldsymbol{U}_m\nabla(\boldsymbol{U}_m)\right] = \beta\nabla\Pi_m + \boldsymbol{M}_v. \tag{2.27}$$

Thus, using equation (2.23):

$$\rho_v\beta\left[\frac{\partial \boldsymbol{U}_m}{\partial t} + \boldsymbol{U}_m\nabla(\boldsymbol{U}_m)\right] = \beta\nabla\Pi_m - \Gamma_v \boldsymbol{U}_m + \boldsymbol{M}_v. \tag{2.28}$$

Equation (2.5) can be also written, scaling all terms by ρ_m/ρ_v, as

$$\rho_m\frac{\partial \boldsymbol{U}_m}{\partial t} + \rho_m \boldsymbol{U}_m\nabla(\boldsymbol{U}_m) = \frac{\rho_m}{\rho_v}\left[\nabla\Pi_m - \frac{\Gamma_v \boldsymbol{U}_m}{\beta} + \frac{\boldsymbol{M}_v}{\beta}\right]. \tag{2.29}$$

Scaling (2.22) by $\boldsymbol{U}_m$ leads to

$$\boldsymbol{U}_m\frac{\partial\rho_m}{\partial t} + \boldsymbol{U}_m\nabla(\rho_m \boldsymbol{U}_m) = 0. \tag{2.30}$$

Thus, summing equations (2.29) and (2.30):

$$\frac{\partial(\rho_m \boldsymbol{U}_m)}{\partial t} + \nabla\left(\rho_m \boldsymbol{U}_m^2\right) = \frac{\rho_m}{\rho_v}\left[\nabla\Pi_m - \frac{\Gamma_v \boldsymbol{U}_m}{\beta} + \frac{\boldsymbol{M}_v}{\beta}\right]. \tag{2.31}$$

Equation (2.31), derived from equation (2.25), is redundant when using equation (2.24) if

$$\frac{\rho_m}{\rho_v}\left[\nabla\Pi_m - \frac{\Gamma_v \boldsymbol{U}_m}{\beta} + \frac{\boldsymbol{M}_v}{\beta}\right] = \nabla\Pi_m$$

or, using $\beta = \frac{\rho_m - \rho_l}{\rho_v - \rho_l}$:

$$\boldsymbol{M}_v = \Gamma_v \boldsymbol{U}_m + \frac{(\rho_m - \rho_l)(\rho_m - \rho_v)}{\rho_m(\rho_v - \rho_l)}\nabla\Pi_m. \tag{2.32}$$

It appears that ignoring equation (2.25) results in treating the momentum fluxes between vapour and liquid implicitly according to equation (2.32). The first term in the expression for $\boldsymbol{M}_v$ corresponds to a momentum transfer directly linked to the mass transfer during vaporization and condensation processes: let us consider inside the volume V an elementary mass δm of liquid moving at velocity $\boldsymbol{U}_m$. If these liquid particles vaporize, δm is transferred from the liquid phase to the vapour one, and the vapour phase also gains the momentum $\delta m \boldsymbol{U}_m$.

The second term in the expression for $\boldsymbol{M}_v$ results from the momentum fluxes due to the inertial effects, i.e. the stresses applied by one phase on the other when the latter accelerates or decelerates. The general expression for this term is given by Ishii (1975):

$$\boldsymbol{M}_{\textit{inertial effects}} = \beta_e \beta(1-\beta)\left[\frac{\mathrm{D}_v \boldsymbol{U}_v}{\mathrm{D}t} - \frac{\mathrm{D}_l \boldsymbol{U}_l}{\mathrm{D}t}\right] \tag{2.33}$$

where β_e is a parameter derived from experiments ($\mathrm{kg\,m^{-3}}$), and $\mathrm{D}_v/\mathrm{D}t$, $\mathrm{D}_l/\mathrm{D}t$ are the Lagrangian derivatives for the vapour and the liquid phases, respectively. Equation (2.32) can also be expressed in the following form:

$$\boldsymbol{M}_v = \Gamma_v \boldsymbol{U}_m + (\rho_l - \rho_v)\beta(1-\beta)\frac{\nabla\Pi_m}{\rho_m}. \tag{2.34}$$

It appears that the no-slip condition significantly simplifies equation (2.33) in the present case: the term $[\mathrm{D}_v \boldsymbol{U}_v/\mathrm{D}t - \mathrm{D}_l \boldsymbol{U}_l/\mathrm{D}t]$ can be identified with $\nabla\Pi_m/\rho_m$, while the parameter β_e here equals $\rho_l - \rho_v$. It means that if a volume of liquid is accelerated, the resistance applied by the adjacent volumes of vapour is transmitted exclusively by the local stress tensor. The forces between vapour and liquid are thus only due to the pressure and the classic viscous stresses, as in a single-phase flow. This leads to the treatment of only equations (2.22), (2.23), and (2.24), which are the basis of most of the cavitation models, although the mass equations are sometimes expressed under in form of equations (2.14) and (2.15), as reported previously. The different approaches differ in practice by the expression for the mass transfer Γ_v.

2.5. *Expression for the mass transfers*

Mass transfers between the two phases are described either by a supplementary equation that controls the convection/production of vapour (Merkle *et al.* 1998; Kunz *et al.* 2000), or by the evolution of a cluster of bubbles according to a simplified Reyleigh–Plesset equation (Kubota *et al.* 1992; Singhal *et al.* 2002), or by a barotropic-state law derived from the model proposed by Delannoy & Kueny (1990).

In the two first cases, the expression for Γ_v is given explicitly, whereas in the case of the barotropic state law it results from the shape of the law. Explicit expressions for Γ_v usually involve the local pressure difference with the vapour pressure. Several expressions of Γ_v were proposed successively by Chen & Heister (1994), Avva, Singhai & Gibson (1995), Reboud & Stutz (1995), Merkle *et al.* (1998), Kunz *et al.*

(2000), and Senocak & Shyy (2004*a*, *b*). Kunz *et al.* proposed splitting Γ_v into two different terms respectively for the vaporization and the condensation:

$$\Gamma_v = m^- + m^+, \tag{2.35}$$

with

$$m^- = \frac{C_{dest}\,\rho_v \beta_l \min(0,\, P - P_v)}{\left(\frac{1}{2}\rho_l U_\infty^2\right) t_\infty} V \qquad \text{(vaporization term)},$$

$$m^+ = \frac{C_{prod}\,\rho_v (\beta_l)^2 (1-\beta_l)}{t_\infty} V \qquad \text{(condensation term)},$$

and

$$C_{dest} = C_{prod} = 100.$$

Other expressions for Γ_v based on the evolution of a cluster of bubbles according to a simplified Rayleigh–Plesset equation were proposed successively by Kubota *et al.* (1992), Yu, Ceccio & Tryggvasan (1995), Hirschi & Dupont (1998), Matsumoto (1998), Sauer & Schnerr (2000), and Singhal *et al.* (2002). Although this formulation is sometimes considered as more physically relevant than the previous one, some serious restrictions should be mentioned: the Rayleigh–Plesset equation is assumed to govern the radius evolution of a single spherical bubble in a pressure field, whereas clouds of vapour are composed of many bubbles that strongly interact with each other, and do not remain spherical. All these explicit expressions for Γ_v are postulated on the basis of physical considerations whose validity depends on the local two-phase flow structure: the expression based on the Rayleigh–Plesset equation is relatively well adapted to clouds of small bubbles, for example in the wake of the sheet cavities, while it should be considered with caution inside the cavity, where the volume fraction of vapour increases up from 30 % to 50 % (Stutz & Reboud 1997*a*, *b*, 2000; Coutier-Delgosha *et al.* 2006). On the other hand, the expressions for Γ_v based on the local value of the pressure leads to reliable results in the areas of cavity growth, since this process is mainly governed by the pressure gradient evolution.

An alternative approach consists of postulating a state law for the mixture, instead of resolving the diffusion equation (2.23). In most such models a barotropic state law is considered, mainly characterized by a high slope in the liquid/vapour mixture where the speed of sound decreases down to a few metres per second (Jakobsen 1964). In this case the mass fluxes between vapour and liquid are not given explicitly, but they depend implicitly on the shape of the state law. The local volume fraction of vapour β is derived from the local value of the medium density ρ_m. So these models correspond to the resolution of the three following equations:

$$\frac{\partial \rho_m}{\partial t} + \nabla(\rho_m \boldsymbol{U}_m) = 0 \qquad \text{(mass equation)}, \tag{2.36}$$

$$\frac{\partial}{\partial \mathrm{t}}(\rho_m \boldsymbol{U}_m) + \nabla(\rho \boldsymbol{U}_m^2) = \nabla \Pi_m \qquad \text{(momentum equation)}, \tag{2.37}$$

$$\beta = f(P) \qquad \text{(state law)}. \tag{2.38}$$

Equations (2.36) to (2.38) result in the treatment of a single-phase flow characterized by a high compressibility, with the density varying from ρ_v to ρ_l. This approach has been used for example by Delannoy & Kueny (1990), Ventikos & Tzabiras (1995), Reboud *et al.* (1998), Song & He (1998), Shin & Ikohagi (1998). It is based on the same main assumptions as the models mentioned previously, but the mass fluxes are

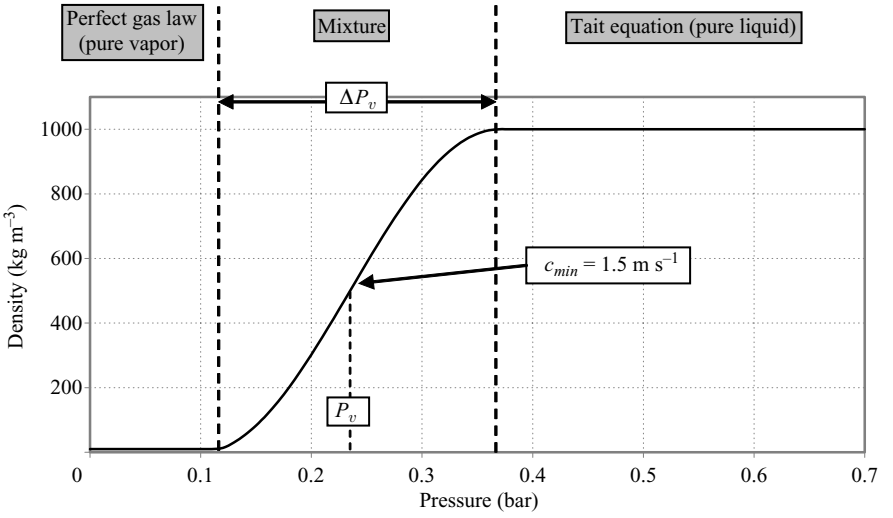

FIGURE 3. Barotropic state law for the mixture.

treated implicitly. So all these models are much closer to each other than is usually suggested. The only significant difference results from the absence of time relaxation in the models based on a state law: the vaporization and condensation processes are instantaneously correlated with the pressure fluctuations, whereas supplementary effects can be added to the explicit expressions for Γ_v. However, these effects usually involve some adjustable parameters (see C_{prod} and C_{dest} in the model proposed by Kunz *et al.*). In the barotropic state law proposed initially by Delannoy (1989), only the maximum slope of the law, i.e. the minimum speed of sound, must be known. The pure liquid and pure vapour areas were considered as incompressible.

The present approach is derived from this initial model: the flow is assumed to be composed of a single fluid whose density varies abruptly from the pure liquid one to the pure vapour one in the vaporized areas. So the liquid/vapour mixture is considered as a homogenous medium whose local density is strongly modified in case of vaporization or condensation. Density variations are controlled with a barotropic state law (figure 3) that links them directly to the pressure field evolution. The state law is mainly composed of three parts:

(i) For a pressure much higher than the vapour pressure P_v (on the right of figure 3), the flow is composed of pure liquid and the Tait state law reported by Knapp, Daily & Hammit (1970) is applied:

$$\frac{\rho_m}{\rho_{\text{ref}}} = \left(\frac{P + P_0}{P^T_{\text{ref}} + P_0} \right)^{1/n} \tag{2.39}$$

where P^T_{ref} is the pressure at the outlet, ρ_{ref} the liquid density, and for water $P_0 = 3 \times 10^8$ Pa and $n = 7$.

(ii) For a pressure much lower than P_v (on the left of figure 3), the fluid is locally completely vaporized and the density is governed by the perfect gas law:

$$\frac{P}{\rho_m} = RT \qquad \text{with } R = 462\,\text{J K}^{-1}\,\text{kg}^{-1}. \tag{2.40}$$

(iii) These two low compressibility configurations are joined in the vapour pressure neighbourhood by a central part whose high slope models the high compressibility of

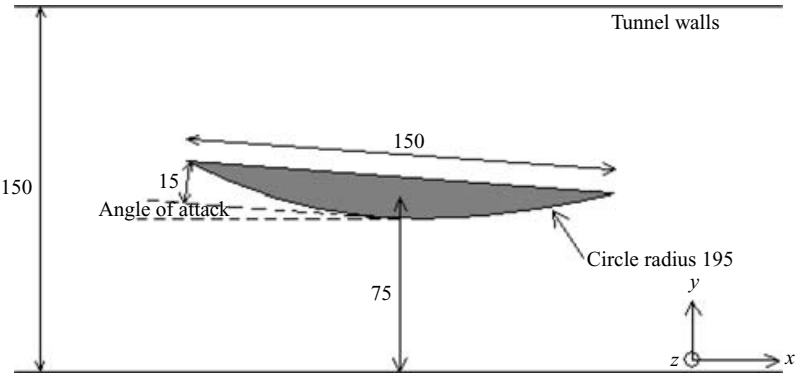

FIGURE 4. Foil geometry (dimensions in mm).

the liquid/vapour mixture. Many equations of state applied to vapour–liquid phase equilibria are available in the literature (Wei & Sadus 2000). Their accuracy has been much improved since the initial law proposed by van der Waals in 1873. However, the cavitating flow is characterized by continuous vaporization and condensation, so thermodynamic equilibrium is never reached between phases. Thus, there is no physical justification for the use of these equations of state.

The shape of this part has only a small influence on the results: only the value of the minimum speed of sound c_{min} (i.e. the maximum slope) is relevant. This parameter is thus derived from the estimated value of the speed of sound in a cavitating area, i.e. about a few metres per second (Jakobsen 1964). $c_{min} = 1.5\,\mathrm{m\,s^{-1}}$ was adopted previously by Coutier-Delgosha *et al.* (2003*a*) as the default value and it is applied in the present study.

3. Experimental device

We consider the cavitating flow on a two-dimensional foil section whose dimensions are 150 mm chord and 80 mm span. Its cross-section is composed of a flat upper surface and a convex lower surface of 195 mm radius, as reported in figure 4. The foil is placed in the ENSTA cavitation tunnel whose test section is of 150 mm height, 80 mm width, and 640 mm length. The foil is located at mid-height, with a small angle of attack, so sheet cavitation appears on the upper face, when the pressure is decreased in the tunnel. Compared with the Venturi configuration studied previously by Stutz & Reboud (1997*a*, *b*, 2000), the cavitation behaviour is modified by the possible interaction between the foil pressure and suction sides. The inner structure of the sheet cavity is investigated at three angles of attack α_i, namely 3°6′, 4°42′ and 5°54′. These values correspond to the actual incidences checked after manufacturing the sidewalls on which the foil is fixed. The uncertainty in α_i can be estimated to 1 %. Note that α_i is expressed in degrees in the text for convenience, but its value is set in radians in all expressions it is involved in hereafter. The values of α_i are consistent with the incidence of the flow at the blade leading edge in an inducer, and the periodic cavity fluctuations obtained in this two-dimensional configuration are representative of the oscillations observed in the three-dimensional turbomachinery.

The cavitating conditions are defined by the value of the cavitation number $\sigma = (P_{\mathrm{ref}} - P_v)/\frac{1}{2}\rho_l U_{ref}^2$ where P_{ref} and U_{ref} denote respectively the static pressure and the mean velocity at the inlet of the test section. P_{ref} is measured with a JPB model TB 142 absolute pressure sensor connected to two pressure taps located

respectively at the bottom and at the top of the test section inlet. U_{ref} is derived from the mass flow rate Q and the size of the cross-section at the inlet. Q is controlled by a propeller flow meter. These flow conditions are regulated with 3 % and 1 % precision respectively for P_{ref} and U_{ref}, which leads to a 5 % uncertainty in the cavitation number σ.

The size of the sheet cavity will hereafter be mainly characterized by its length L_{cav}. L_{cav} refers in the present work to the attached part of the vaporized area only, without considering the clouds of vapour detached from the foil. Although L_{cav} fluctuates in unsteady conditions, because of the periodic vapour shedding, a mean length can be estimated visually using signs painted on the foil surface each 5 mm. This method has been compared by Coutier-Delgosha *et al.* (2005) to the lengths obtained by averaging respectively 60 side views and 60 top views of the cavity, and a maximum discrepancy of 8 % was obtained.

An X-ray absorption device is applied to investigate the local volume fraction of the vapour phase inside the cavity and in the wake. The experiments were carried out as a collaboration between the ENSTA laboratory and the CEA (French Atomic Energy Commission). A 160 kV/1 mA X-ray generator was used to emit radiation from one vertical side of the cavitation tunnel (figure 5), while 24 detectors running in current mode measured the X-ray intensity on the opposite side, from the foil leading edge to the trailing edge. This method enables the determination of the instantaneous quantity of vapour in the volumes crossed by the X-rays from the generator to each detector, according to the following equation:

$$\frac{V_v(t)}{V} = 1 - \frac{\ln(I_0/I(t))}{\ln(I_0/I_1)} \tag{3.1}$$

where $V_v(t)$ is the instantaneous volume of vapour, V is the total volume, and I_0 (I_1) is the intensity detected when the measurement volume V is empty (full) of pure liquid. Fast data acquisitions at 1000 Hz are performed in order to detect the evolution of the volume fraction associated with the flow instability. This method was applied previously by Stutz & Legoupil (2003) in the configuration of sheet cavitation at the throat of a Venturi-type section, to study the evolution of the amount of vapour from the upstream end to the downstream end of the cavity. In their work no information was available concerning the distribution of the volume fraction in the cavity height, whereas in the present case the detectors have also been discretized in the vertical y direction, in order to obtain instantaneous maps of the volume fraction: the 24 Na(TI) detector width and height are 8 mm and 4 mm, which results in mean dimensions for volumes V equal to 6×3 mm (in the middle of the cavitation tunnel, see figure 5). The successive measurements in the y direction are obtained by moving the whole setup vertically (generator and detectors). The X-ray source is characterized by a rectangular collimator (2×35 mm) and its operating conditions are 160 kV − 1 mA. The focal length of the fan beam collimator is 715 mm (0.85° aperture for each detector). No filtering is applied to the measurements presented here. For each position of the detectors, the acquisition was performed during 30 s, so 30 000 data points were obtained.

X-ray measurements are characterized by an uncertainty based on the following expression:

$$\delta\left(\frac{V_v(t)}{V}\right)^2 = \left[\frac{\ln(I/I_1)}{I_0(\ln(I_0/I_1))^2}\right]^2 \delta I_0^2 + \left[\frac{\ln(I_0/I)}{I_1(\ln(I_0/I_1))^2}\right]^2 \delta I_1^2 + \left[\frac{1}{I(\ln(I_0/I_1))}\right]^2 \delta I^2. \tag{3.2}$$

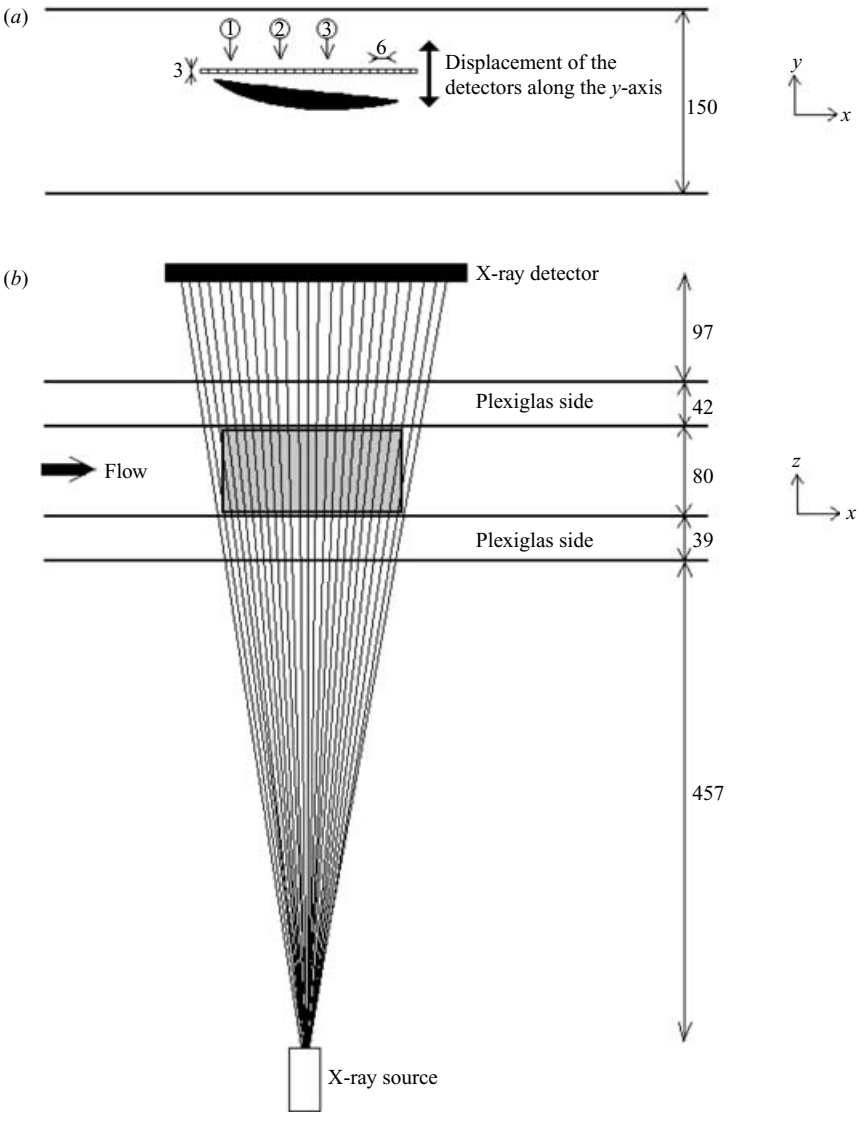

FIGURE 5. Illustration of the X-ray attenuation device: (*a*) side view, (*b*) top view (dimensions in mm).

This leads in the case of the 3°1 incidence to a maximum relative error lower than 5 % with a level of confidence equal to 68 %. The uncertainty is slightly higher for the incidences 4°7 and 5°9 (respectively 11 % and 12 %) because the signal intensity was lower than in the first case. This decrease can be attributed to a minor anomaly in the X-ray source and/or functioning of the detectors.

The pressure fluctuation signal is also recorded to detect the successive vapour cloud shedding and to facilitate the connection between the data obtained at the different positions in the vertical direction. Measurements are performed with a PCB model M106B50 piezo-electric pressure transducer whose resonant frequency is 40 kHz and sensibility is 0.07 mV Pa^{-1}. The transducer is mounted flush in one of the vertical walls of the test section, 30 mm upstream of the foil leading edge.

Data set 1			Data set 2 (X-ray measurements)								
α_i	σ	U_{ref}	α_i	σ	U_{ref}	α_i	σ	U_{ref}	α_i	σ	U_{ref}
1° to 6°	0.5	6	3°1′	0.5	6	4°7′	0.8	6	5°9′	0.95	6
	0.7	6	3°1′	0.7	6	4°7′	0.95	6	5°9′	1.15	6
	0.9	6	3°1′	0.9	6	4°7′	1.2	6	5°9′	1.4	6
	1.1	6	3°1′	1.1	6	4°7′	1.4	6	5°9′	1.2	5
	1.3	6	3°1′	0.8	5	4°7′	1	5	5°9′	1.2	7
	1.6	6	3°1′	0.8	7	4°7′	1	7	5°9′	1.2	8
	1.8	6	3°1′	0.8	8	4°7′	1	8			
			3°1′	0.8	9						

TABLE 1. Flow conditions for the two sets of experimental data.

Two sets of experimental data are presented (see table 1). They were obtained with different experimental procedures:

Set 1 was obtained a few months before the X-ray measurements. So, for each flow condition, only the mean cavity length L_{cav} and the shedding frequency f were recorded. The angle of attack was varied between 0° and 6° by steps of 1°, the reference velocity U_{ref} was equal to $6\,\mathrm{m\,s^{-1}}$, and a large range of cavitation numbers was tested, from $\sigma = 1.8$ down to $\sigma = 0.5$. This set of data has been used by Coutier-Delgosha *et al.* (2005) and it will be considered in the present paper as the reference one.

Set 2 corresponds to the X-ray measurements. Three angles of attack were tested: 3°1, 4°7, and 5°9. U_{ref} is varied from $5\,\mathrm{m\,s^{-1}}$ to $9\,\mathrm{m\,s^{-1}}$, and σ is varied from 0.5 to 1.4 to obtain several cavity lengths at each incidence. For a single value of σ (corresponding to L_{cav}/L_{ref} close to 0.75), U_{ref} is varied from $5\,\mathrm{m\,s^{-1}}$ to $9\,\mathrm{m\,s^{-1}}$, to investigate the effect of the flow velocity on cavitation.

4. Numerical model

The resolution of the unsteady Reynolds-averaged Navier–Stokes equations is coupled with the physical model of cavitation presented in § 2. The main features of the solver are given next, and additional details can be found in Coutier-Delgosha *et al.* (2003*a*).

4.1. *Algorithm*

Two-dimensional calculations are performed. Although the foil aspect ratio is close to 0.5, top views of the cavitating flow show that the sidewalls of the cavitation tunnel have only a moderate influence on the sheet cavity shape in the spanwise direction: about 15 mm on each side is affected, while the foil span is 80 mm. So, it is expected that the present configuration is governed mainly by two-dimensional effects that two-dimensional calculations should be reproducible.

According to the state law applied to the mixture, density depends only on the pressure. This means that thermal effects are neglected and no energy equation is considered. Such an assumption is completely valid for cavitation in cold water: the variation of P_v due to the slight cooling of the flow in the vaporized areas (about 1.4 Pa, according to Charles 1994) is negligible compared to the ΔP_v range represented in figure 3 (about 3000 Pa).

The mass and momentum equations are solved in the orthogonal frame of curvilinear coordinates (ξ, η), which leads to the following system of equations:

$$\left.\begin{aligned} &S\frac{\partial}{\partial t}(\rho\Phi) + \nabla_\xi\left(\rho u\Phi - \Gamma_\Phi\frac{\partial\Phi}{\partial\xi}\right) + \nabla\eta\left(\rho v\Phi - \Gamma_\Phi\frac{\partial\Phi}{\partial\eta}\right) = S_\Phi \\ &\rho = F(C_p, \sigma), \end{aligned}\right\} \tag{4.1}$$

where u and v are the velocity components along coordinates ξ and η respectively, Φ stands either for 1, u or v, Γ_Φ is the diffusion coefficient, ∇_ξ and ∇_η are the physical components of the divergence operator along the curvilinear coordinates, S_Φ is the source term, C_p is the non-dimensional pressure coefficient, and σ is the cavitation number.

The numerical resolution is based on a pressure correction method derived from the SIMPLE algorithm proposed by Patankar (1981). The coupling between the Reynolds equations and the highly compressible state law has induced several modifications of the initial scheme (Coutier-Delgosha *et al.* 2003*a*). Each physical time step consists of successive iterations which march the solution towards convergence. A finite-volume discretization is applied, associated with a staggered grid to avoid pressure oscillations. The diffusive terms are calculated in a purely central manner, while the convection terms are estimated with the non-oscillatory second-order HLPA (hybrid linear/parabolic approximation) scheme proposed by Zhu (1991). This is a second-order scheme, which locally switches to first order, to prevent numerical oscillations in critical high-pressure- or high-density-gradient areas. A second-order implicit time integration scheme is applied:

$$\frac{\partial(\rho\Phi)}{\partial t} = \frac{1.5\rho^{n+1}\Phi^{n+1} - 2\rho^n\Phi^n + 0.5\rho^{n-1}\Phi^{n-1}}{\Delta t}. \tag{4.2}$$

The main steps of a single iteration are listed next:

(i) Resolution of the transport equations for the turbulent variables, and calculation of the turbulent viscosity ν_t.

(ii) Calculation of the estimated velocities $\boldsymbol{U}^*(u^*, v^*)$ from the momentum balance equations.

(iii) Calculation of the density ρ^* and its derivative $(\partial\rho/\partial P)$, according to the barotropic state law.

(iv) Resolution of the pressure correction equation. It is derived from the mass balance equation, which is discretized in each cell according to the following expression:

$$1.5\frac{S}{\Delta t}\rho_p^{n+1} = -\rho_e^{n+1}u_e^{n+1}\Delta\xi_e + \rho_w^{n+1}u_w^{n+1}\Delta\xi_w - \rho_n^{n+1}v_n^{n+1}\Delta\eta_n + \rho_s^{n+1}v_s^{n+1}\Delta\eta_s + S_\rho^n \tag{4.3}$$

where S is the cell area, p denotes the current cell, and e, w, n, s denote the east, west, north, and south neighbouring cells. S_ρ^n contains the explicit source terms resulting from the time discretization.

To obtain the final pressure correction equation, velocities u and v are replaced by $u^* + \mathrm{d}u$, $v^* + \mathrm{d}v$, respectively, while ρ is replaced by $\rho^* + \mathrm{d}\rho$. Thus, the pressure correction equation yields not only velocity variations $\mathrm{d}\boldsymbol{U}(\mathrm{d}u, \mathrm{d}v)$ but also supplementary terms involving variations $\mathrm{d}\rho$. The term $\mathrm{d}\boldsymbol{U}$ is derived from a simplified differential form of the momentum balance equation, while $\mathrm{d}\rho$ is written

$$\mathrm{d}\rho_{i,j} = \left(\frac{\partial\rho}{\partial P}\right)_{i,j}\mathrm{d}P_{i,j}. \tag{4.4}$$

(v) When the pressure correction $\mathrm{d}P$ is obtained, not only the velocity and the pressure but also the density values are corrected, according to the following expression:

$$\rho = \rho^* + \left(\frac{\partial \rho}{\partial P}\right)\mathrm{d}P. \tag{4.5}$$

Densities obtained from equation (4.5) may be outside the physical range, because of the high local values of $(\partial\rho/\partial P)$ in the two-phase mixture. Non-physical values are thus corrected, and a supplementary loop over the pressure correction step is performed until all values of the void ratio are obtained inside their physical range [0, 1].

4.2. *Turbulence model*

The Reynolds number based on U_{ref} and the chord L_{ref} varies between 8×10^5 and 1.4×10^6 in the experiments, so the flow is fully turbulent in almost all the vaporized areas, and a turbulence model is applied in the numerical simulations. As reported by Yuan & Schnerr (2003) and Coutier-Delgosha *et al.* (2003*a*), simulating cloud cavitation with a standard two-equation turbulence model encounters serious difficulties, since turbulent dissipation is systematically over-estimated in the rear part of the cavitation sheet. As a result, the re-entrant jet is stopped before breaking the cavity interface, and the flow remains stable. Corrections are usually applied to these models to obtain unsteady sheet cavitation. Wu, Wang & Shyy (2005) propose for example applying a filter-based k–ε model. In this approach, the filter depends on the grid size, in order to avoid excessive dissipation in small-scale motions, without altering the large-scale flow characteristics. In the case of the barotropic state law, Coutier-Delgosha, Fortes–Patella & Reboud (2003*b*) have shown that taking into account the effect of the liquid/vapour mixture compressibility on the turbulence structure is necessary to obtain the unsteady effects reported in experiments. So the modification of the k–ε RNG turbulence model proposed in that previous publication is applied in the present calculations. The turbulent viscosity is expressed in the form

$$\mu_t = f(\rho) C_\mu k^2/\varepsilon, \tag{4.6}$$

with

$$f(\rho) = \rho_v + (1-\beta)^n(\rho_l - \rho_v), \quad n = 10, C_\mu = 0.085, \tag{4.7}$$

where k denotes the turbulent energy, and ε the turbulent dissipation. All parameters of the model, except the function $f(\rho)$, are set to the value proposed by Orszag (1993). According to equation (4.7), f equals ρ_v or ρ_l in the regions containing respectively pure vapour or pure liquid, but it decreases rapidly toward ρ_v for an intermediate volume fraction of vapour. This modification has been applied previously in several configurations (Venturi-type sections, foil sections, cascade of hydrofoils) and a correct simulation of the unsteady flow properties was obtained in all situations (Coutier-Delgosha, Fortes-Patella & Reboud 2002). A similar improvement was achieved by using the corrections proposed by Wilcox (1998) in his k–ω model compressible fluids (Coutier-Delgosha *et al.* 2003*b*).

4.3. *Boundary conditions, initial conditions, convergence criteria and grid*

The length of the computational domain in the flow direction is $5L_{ref}$ downstream from the foil section and $2L_{ref}$ upstream. These dimensions were found in previous studies to be large enough to minimize the influence of the inlet and outlet boundary conditions on the behaviour of the cavitating flow. Although the flow in the vaporized

Grid size	Δt	σ	L_{cav}/L_{ref}	f (Hz)	Mean vapour volume ($\times 10^{-4}$ m^3)
140×70	$T_{ref}/50$	1.19	0.35	32.6	1.95
140×70	$T_{ref}/100$	1.20	0.4	26.7	2.51
140×70	$T_{ref}/200$	1.22	0.42	26.4	2.74
140×70	$T_{ref}/500$	1.22	0.42	26.3	2.75
70×40	$T_{ref}/200$	1.17	0.325	35.2	1.67
100×50	$T_{ref}/200$	1.19	0.4	29.6	2.61
350×90	$T_{ref}/200$	1.19	0.42	26.3	2.69
540×90	$T_{ref}/200$	1.22	0.42	26.1	2.70
Experiment		1.2	0.4	26.5	2.64

TABLE 2. Influence of the grid size and the time-step on the mean vapour volume per width unit. (Incidence 4°7′, $\sigma = 1.2$, $L_{cav}/L_{ref} \approx 0.40$, $U_{ref} = 6\,\mathrm{m/s^{-1}}$).

areas is highly compressible, low compressibility conditions are encountered in the pure liquid areas, i.e. in the main part of the domain. So classical boundary conditions for such flow conditions are applied: imposed inlet velocity, and fixed outlet static pressure. Standard 'log-law' wall functions are used along the tunnel walls and the foil surface, so the first grid points are located at a non-dimensional distance from the walls y^+ varying between 25 and 80.

In the simulations, a preliminary stationary step is first performed in non-cavitating conditions: a high pressure level is imposed at the domain outlet, to avoid any flow vaporization. Then, the outlet pressure is decreased slowly during the first hundred time steps, to reach the desired value of the cavitation number σ. Liquid passing over the foil suction side progressively vaporizes during this decrease. The outlet pressure is then kept constant and the calculation is continued for $100T_{ref}$, where $T_{ref} = L_{ref}/U_{ref}$. So the order of magnitude of T_{ref} is the transit time of the flow from the leading edge to the trailing edge of the foil section. When U_{ref} is varied from $5\,\mathrm{m\,s^{-1}}$ up to $9\,\mathrm{m\,s^{-1}}$, $100T_{\mathrm{ref}}$ corresponds to 1.5 s to 3 s, which is sufficient to obtain tenths of cavitation cycles and thus to characterize the flow behaviour (mean attached cavity length L_{cav}, oscillation frequency f). The time-step Δt equals $T_{\mathrm{ref}}/200$, because lower values were found to change the results only slightly, as can be seen in table 2. A detailed study of the influence of the numerical parameters on the unsteady flow behaviour can be found in Coutier-Delgosha *et al.* (2003*a*).

The convergence criterion for each time step and each equation is based on the sum of the absolute values of the residuals in the entire computational domain. This sum must be lower than 10^{-4} for the mass and momentum equations and 10^{-3} for the k and ε equations. Moreover, variations of the non-dimensional density ρ/ρ_l must be lower than 10^{-5}. When all these conditions are fulfilled, the time step is converged.

The grid used for the results presented in § 5 is composed of 140×70 orthogonal cells (figure 6). Four other meshes composed respectively of 70×40, 100×50, 350×90, and 540×90 cells have also been tested for a single flow condition (angle of attack 4°7, $\sigma \approx 1.2$, $U_{ref} = 6\,\mathrm{m\,s^{-1}}$), and the results are compared in table 2. Note that the cavitation number σ is slightly different for each calculation, because the pressure is fixed at the domain outlet, so the upstream pressure fluctuates during the simulations, and σ cannot be imposed strictly. Results reported in table 2 show that increasing the grid size above 140×70 cells does not significantly modify the flow behaviour. This confirms the conclusion previously reported by Coutier-Delgosha

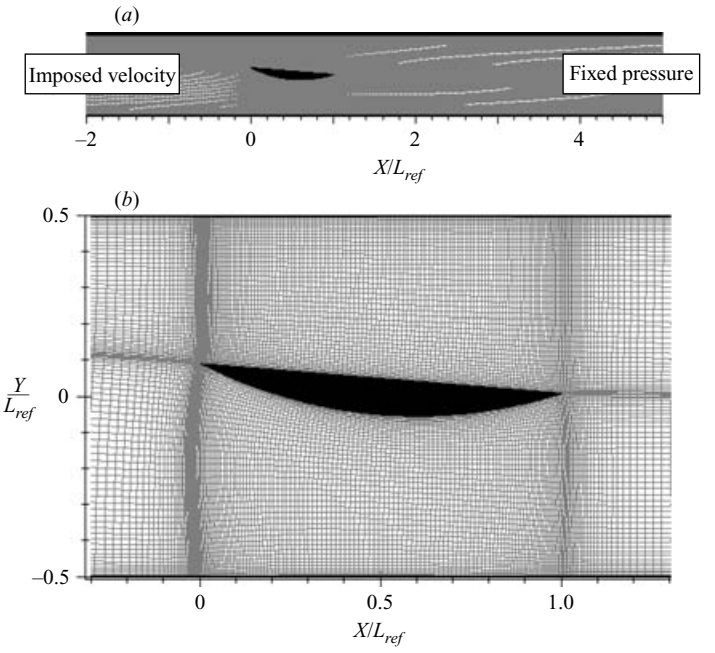

FIGURE 6. Computational grid for the incidence 5°9′ ($L_{ref} = 15$ cm).

et al. (2003*a*) in configurations of Venturi-type sections. A special grid contraction is applied in the areas where cavitation is expected, i.e. on the foil suction side and especially near the leading edge. Section 6 is based on the calculations performed with the finest grid, to discuss the subtle features of the flow.

5. Structure of the vaporized areas

The unsteady behaviour of the sheet cavity is reported qualitatively in figure 7 in the case of a 3°1′ angle of attack, an inlet velocity $U_{ref} = 6\,\mathrm{m\,s^{-1}}$, and a maximum cavity length L_{cav}/L_{ref} close to 0.4. The sheet cavitation destabilization appears clearly in steps 2 and 3, leading to the formation and detachment of a vapour cloud (step 4). This main separation is followed by small detachments (step 5), which finally all collapse in the cavity wake (step 6).

The internal structure of the sheet cavity is investigated here by simulations and experiments. The time-average composition of the cavity and the unsteady properties of the flow are successively considered.

5.1. *Time-average composition*

In this section, the time-average properties of the flow are first investigated. Figures 8(*a*) and 8(*b*) give the evolution of the cavity length according to the parameter σ/α_i, derived from that ($\sigma/2\alpha_i$) proposed by Acosta (1955) in his linearized theory of partial cavitation on flat plate hydrofoils. Le *et al.* (1993) have more recently correlated the cavity length L_{cav} with the parameter σ/α_i, in the case of hydrofoils similar to the present one. The two sets 1 and 2 of experimental data are reported in figure 8(*a*). As it was previously mentioned by Coutier-Delgosha *et al.* (2005), the cavity lengths measured in all flow conditions are very close to a common curve, which suggests that they only depend on σ/α_i. The data scattering may be mainly

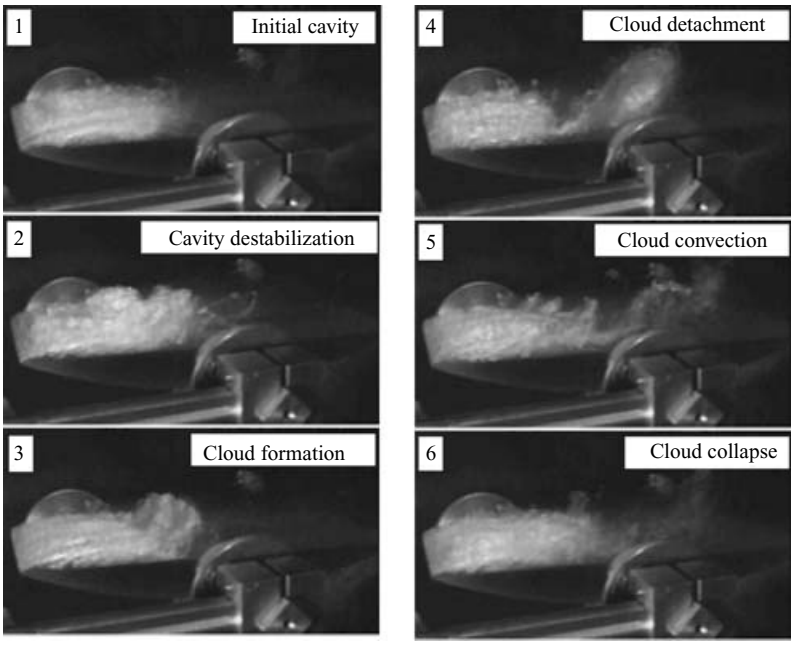

FIGURE 7. Successive shapes of the cavitation sheet during one period of oscillation (incidence $3°1'$, $U_{ref} = 6\,\mathrm{m\,s^{-1}}$, $L_{cav}/L_{ref} \approx 0.4$.)

due to the 8 % measurement uncertainty in L_{cav}. Recall also that the experimental uncertainties in α_i and σ are 1 % and 5 % respectively, so the uncertainty in σ/α_i is 6 %. The solid line is a polynomial approximation of the experimental points of set 1 given by

$$\frac{L_{cav}}{L_{ref}} = \frac{A}{(\sigma/\alpha_i)^n} \tag{5.1}$$

with $A \approx 100$ and $n \approx 2$.

The two sets of data are in close agreement, which shows that the conditions of sheet cavitation that are investigated here by X-ray measurements (set 2) are consistent with the previous measurements published in Coutier-Delgosha *et al.* (2005) with a broader range of flow conditions (set 1).

Measurement set 1 is also compared in figure 8(*b*) to the results of the numerical simulations. To obtain the time-averaged cavity length from the simulations, first the time-averaged density field is calculated, then a threshold value of $\overline{\beta} = 5\,\%$ is applied to find the limit of the sheet cavity (cavitation detached from the foil surface is not considered, as in the experiments). A fair agreement is generally obtained: only very small cavities ($L_{cav}/L_{ref} < 0.15$) are noticeably underestimated by the model. This discrepancy can be associated with a complete and unrealistic stabilization of the flow in the simulations for such small cavity lengths. Figures 8(*a*) and 8(*b*) show that identical flow conditions applied in the experiments and in the simulations lead to similar cavitating conditions. This result enables more precise comparison of the morphology of sheet cavities obtained from X-ray measurements (set 2) and from the simulations, respectively.

Figures 9, 10, and 11 present the experimental time-average distribution of the volume fraction of the vapour phase $\overline{\beta}$ at incidences $3°1'$, $4°7'$, and $5°9$, respectively. For each angle of attack, the results are given for two cavity lengths: a small one

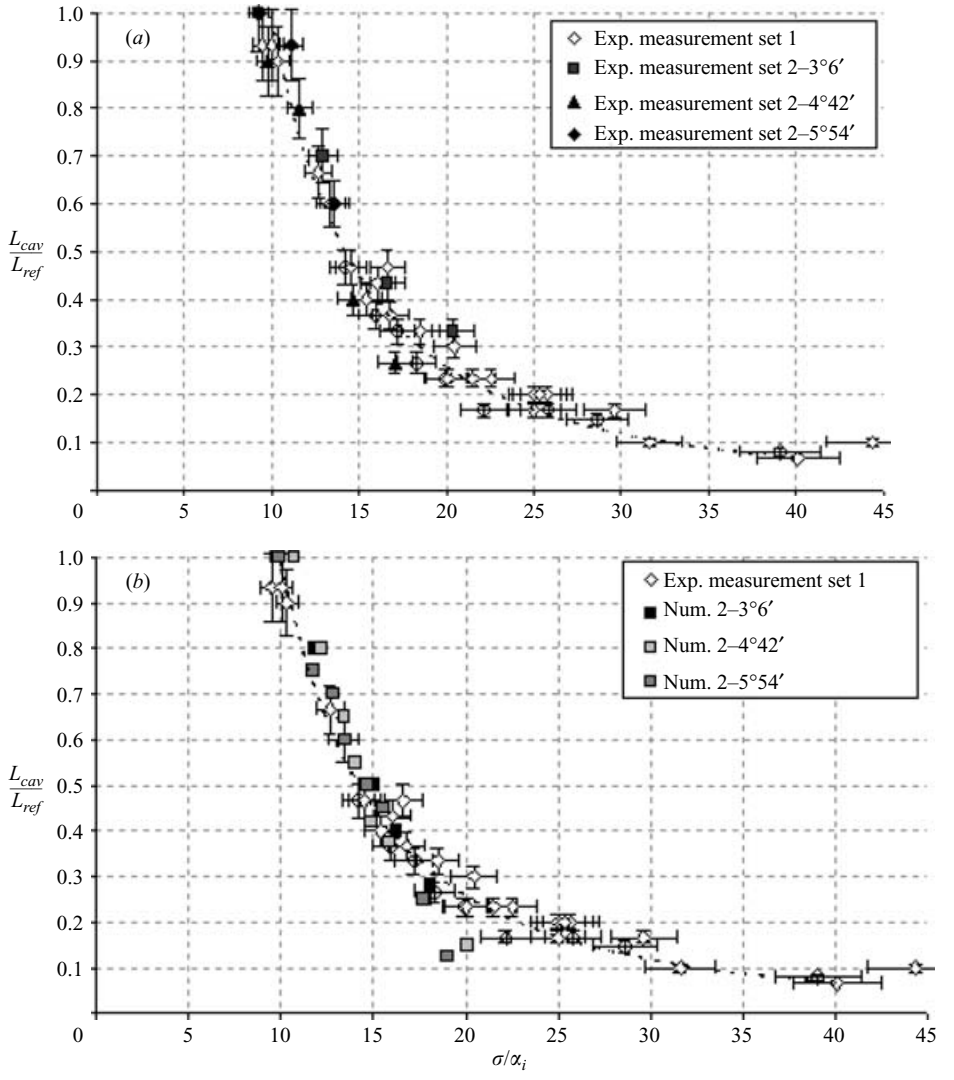

FIGURE 8. Time-average cavity length as a function of σ/α_i for $U_{ref} = 6\,\mathrm{m\,s^{-1}}$: (*a*) comparison between experimental data of set 1 and set 2, (*b*) comparison between the numerical results and the data of set 1.

($L_{cav}/L_{ref} \approx 0.5$) and a large one ($L_{cav}/L_{ref} > 0.7$). The white rectangle on the pictures denotes the limit of the X-ray measurements in the middle of the channel (the square would be larger close to the detectors and smaller close to the X-ray source). At incidence 5°9′, the size of this domain is smaller than at incidence 3°1′ and 4°7′, because of defective detectors in the rear part of the cavity. So for this particular angle of attack, no information is available concerning the cavity wake. X is the horizontal distance from the foil leading edge, while Y denotes the vertical distance from the foil axis of rotation, which is located at the middle of the test section (see figure 4). Note also that the scale of $\overline{\beta}$ is adjusted on the different figures to improve the contrasts. To display the quantitative evolutions of $\overline{\beta}$, three profiles are also indicated, at 2 cm, 5 cm, and 8 cm from the leading edge, respectively. Identical

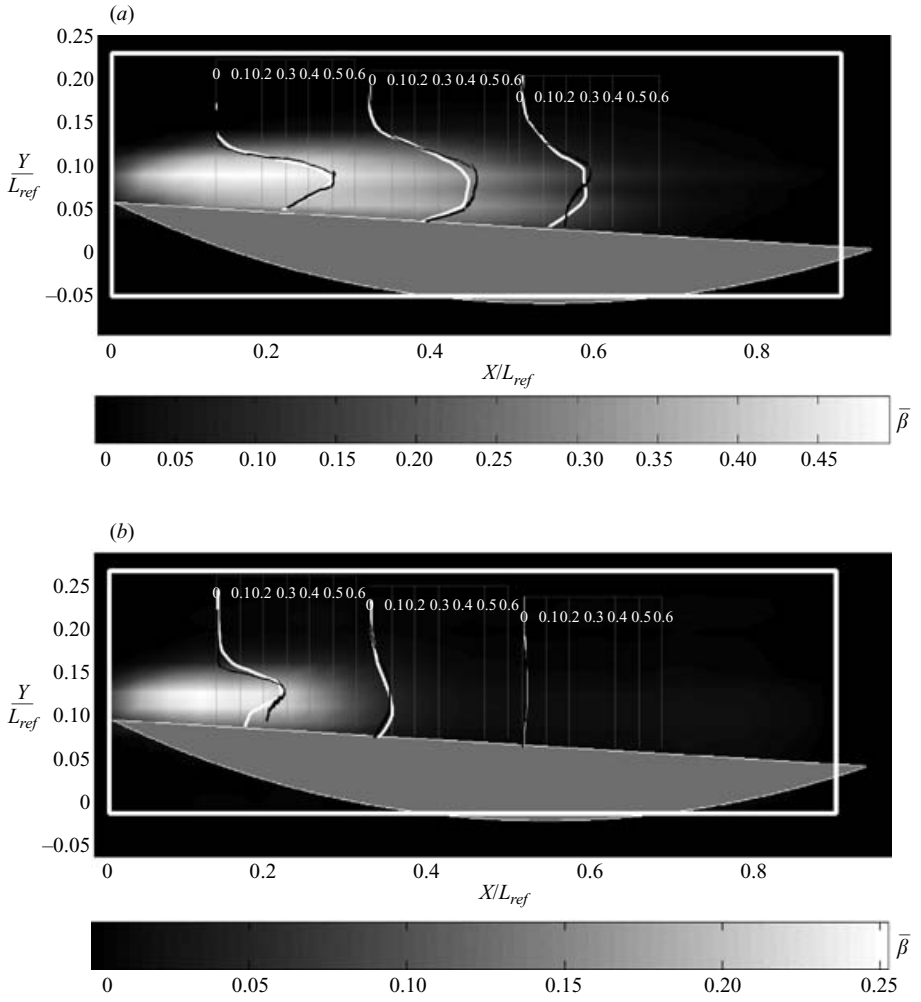

FIGURE 9. Time-average distribution of the volume fraction of the vapour phase $\overline{\beta}$ obtained by experiments at incidence 3°1′ and $U_{ref} = 6\,\mathrm{m\,s^{-1}}$ (measurement set 2). (*a*) $\sigma = 0.7$ ($L_{cav}/L_{ref} \approx 0.7$), (*b*) $\sigma = 0.9$ ($L_{cav}/L_{ref} \approx 0.45$). The large white rectangle denotes the limit of the measurements. The evolution of $\overline{\beta}$ along three vertical profiles (thick white lines) is also compared to the numerical prediction (thin grey lines).

scales are applied, with a maximum volume fraction of 60 %. Both experimental and numerical profiles are reported.

It can be noticed that some vapour is detected at incidences 4°7′ and 5°9′ upstream from the leading edge. This is due to the divergence of the X-rays from the source to the detectors (see figure 5), which makes the measurement volumes change in size and position across the channel. The $\overline{\beta}$ distributions in figures 9 to 11 correspond to their size and position at the middle of the channel. So, measurements volumes represented just upstream from the leading edge have partially crossed the sheet cavity between the front vertical side and the middle of the cavitation tunnel. This is not the case at incidence 3°1′, because the measurement domain was moved slightly downstream.

The time-average volume fraction of the vapour phase $\overline{\beta}$ never exceeds $\overline{\beta}_{\max} = 35\,\%$ in the small cavities, and $\overline{\beta}_{\max} = 60\,\%$ in the large ones. It is lower than 10 % in

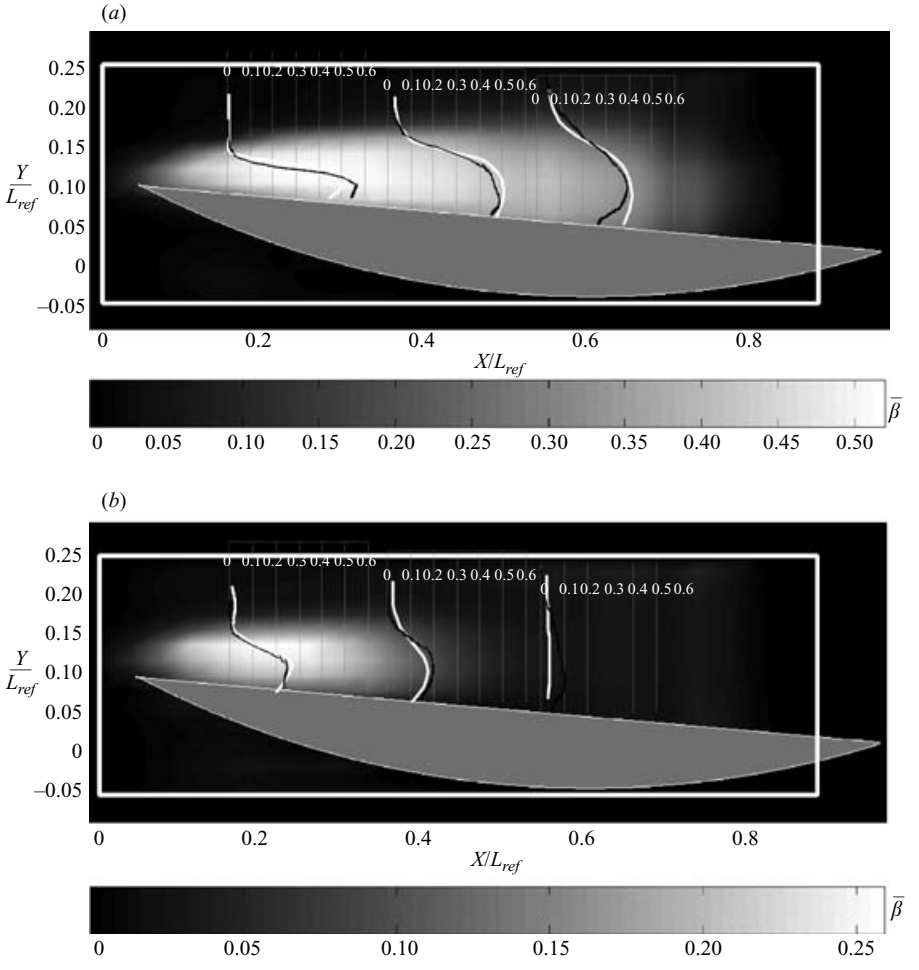

FIGURE 10. As figure 9 but at incidence 4°7′ and (*a*) $\sigma = 0.8$ ($L_{cav}/L_{ref} \approx 0.9$), (*b*) $\sigma = 1.2$ ($L_{cav}/L_{ref} \approx 0.4$).

the cavity wake, where the presence of vapour is hardly detected visually during the experiments. This confirms the results previously obtained by Stutz & Reboud (1997*b*, 2000) for sheet cavitation developed at the throat of Venturi-type sections: they found maximum values lower than 50 % in all cases. Each volume fraction profile exhibited here presents a maximum value at mid-height of the cavity, and then a rapid decrease to zero for both smaller and greater heights. The values obtained by X-ray measurements very close to the foil surface should be considered with caution because the X-ray source was not aligned with the foil incidence, so the volumes crossed by the X-rays partially include a part of the foil. However, a significant decrease of $\overline{\beta}$ close to the foil is systematically obtained.

A fair agreement is obtained between the experimental and numerical results at incidences 3°1′ and 4°7′: both the magnitude of $\overline{\beta}$ and its evolution in the cavity height are close to the measurements. At incidence 5°9′, some notable discrepancies are obtained: all volume fractions predicted by the simulations are lower than the measured one. These discrepancies are observed even for very low values of $\overline{\beta}$, close to the cavity limit for example. Moreover, experimental data exhibit a residual volume

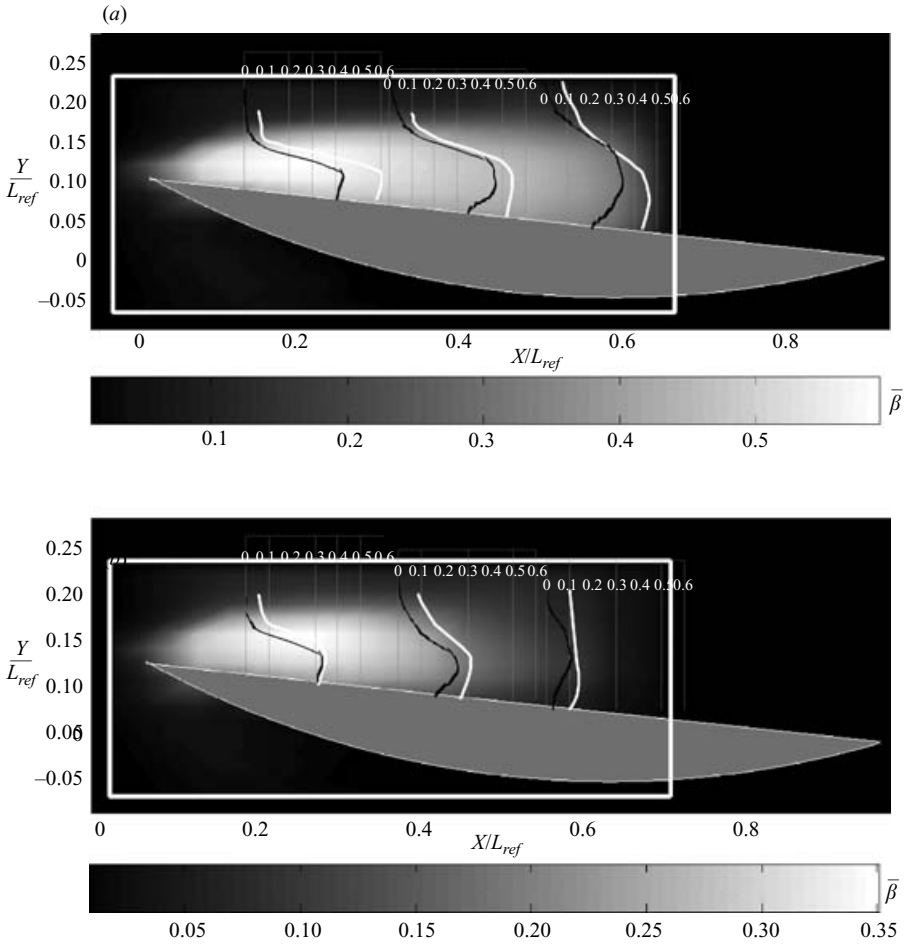

FIGURE 11. As figure 9 but at incidence 5°9′ and (*a*) $\sigma = 0.95$ ($L_{cav}/L_{ref} \approx 1.00$), (*b*) $\sigma = 1.4$ ($L_{cav}/L_{ref} \approx 0.6$).

fraction $\overline{\beta}$ close to 5 % well over this limit, which is not the case at the two other incidences. These observations suggest that a spurious gap $\Delta\beta \approx 5\,\%$ may alter the experimental results at incidence 5°9′. However, no evidence of a further uncertainty on the measurements in this particular case was detected.

The influence of the angle of attack on the maximum time-average volume fraction of the vapour phase $\overline{\beta}_{\max}$ is presented in figure 12(*a*). The data plots are for various cavity lengths, at constant $U_{ref} = 6\,\mathrm{m\,s^{-1}}$. $\overline{\beta}_{\max}$ increases linearly with the cavity length, and the values nearly follow the law $\overline{\beta}_{\max} \approx 0.6 L_{cav}/L_{ref}$. No significant influence of the angle of attack is observed.

A different conclusion arises from figure 12(*b*), which shows the evolution of the time-averaged vapour volume $\overline{V_v}$ contained in the sheet cavity as a function of incidence. The volumes are given here per width unit in order to enable comparisons with the two-dimensional numerical results. The vapour volume also increases linearly with the cavity length, and a close agreement is obtained between the experimental and the numerical results. A significant effect of the incidence is observed here: all values closely follow the law $\overline{V_v} \approx 7 \times 10^{-3} \alpha_i^{0.4} L_{cav}/L_{ref}$, with α_i in degrees. Figures 12(*a*) and

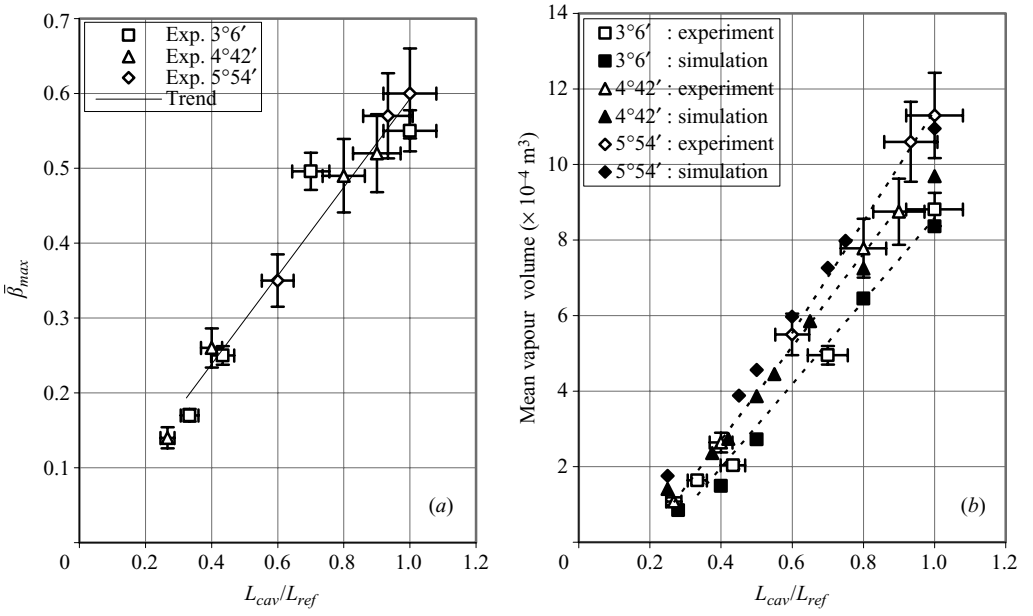

FIGURE 12. Influence of the angle of attack on (*a*) $\overline{\beta}_{max}$ (maximum value of $\overline{\beta}$ in the flow) and (*b*) the time-average vapour volume ($U_{ref} = 6$ m s^{-1}, measurement set 2).

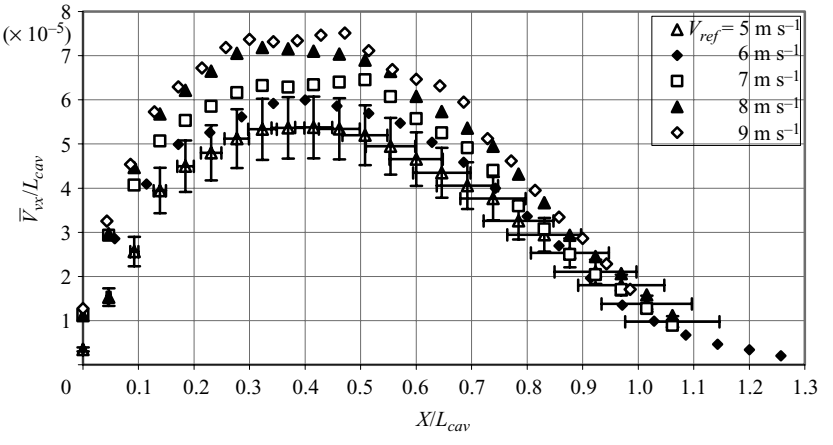

FIGURE 13. Influence of velocity on the evolution of the time-average vapour volume in the flow direction ($\alpha_i = 3°1'$, measurement set 2).

12(*b*) suggest that the angle of attack of the foil may have some influence on the volume fraction distribution inside the cavity. This point is discussed below.

The time-average composition of the sheet cavity is investigated in more detail in figures 13 to 17. Figure 13 focuses on the evolution of the mean vapour volume $\overline{V_{vX}}(X)$ in the flow from the foil leading edge to its trailing edge, at incidence 3°1′. $\overline{V_{vX}}$ at station X corresponds to the vapour volume contained in a cross-section located at point X, per unity of width and depth. The velocity was varied from 5 m s^{-1} to 9 m s^{-1}. The objective is to compare sheet cavities of identical sizes, but in practice the plots are related to cavity lengths L_{cav}/L_{ref} between 0.7 and 0.9. To get rid of this slight

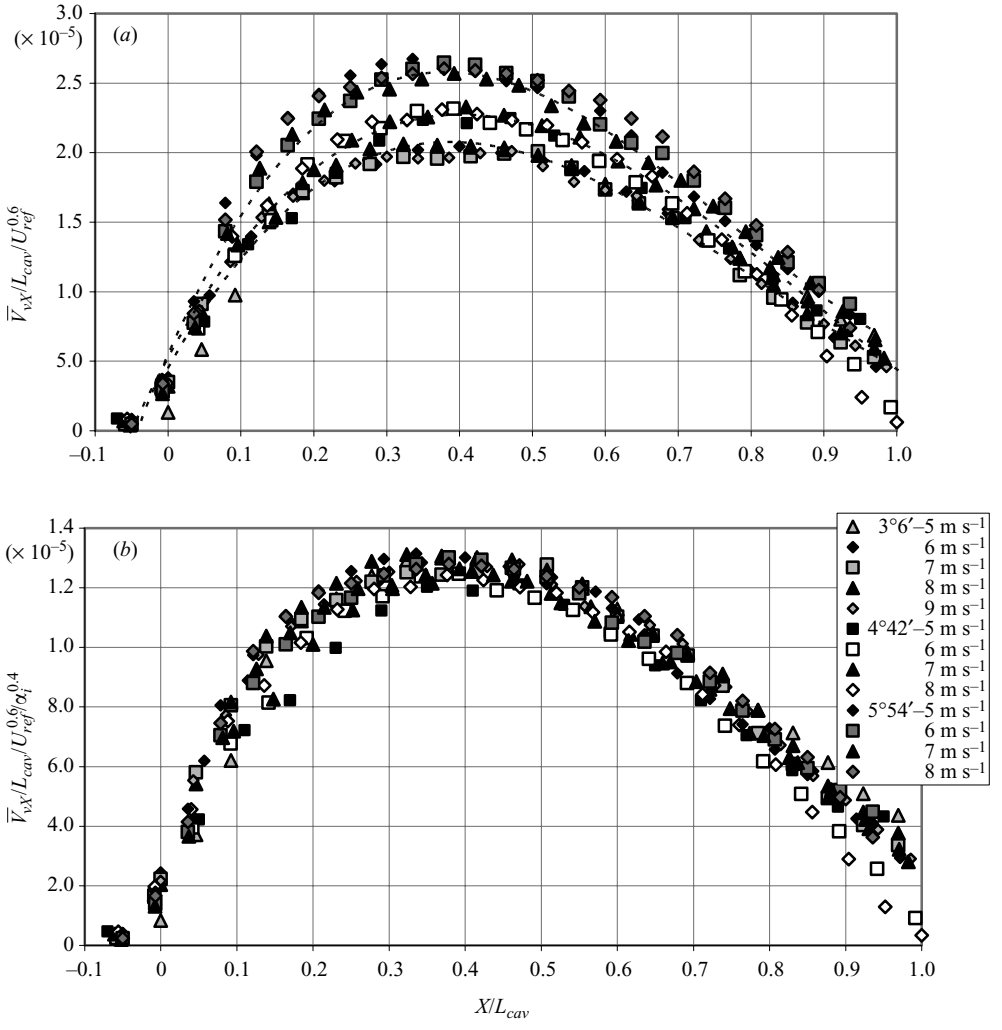

FIGURE 14. Evolution of the vapour volume from the leading edge for to the trailing edge for incidences 3°1′, 4°7′, and 5°9′ (measurement set 2).

inconsistency, $\overline{V_{v\,X}}$ is divided by L_{cav} and plotted as a function of X/L_{cav}. A significant influence of velocity can be observed: $\overline{V_{v\,X}/L_{cav}}$ progressively increases when U_{ref} is increased. On the other hand, the maximum vapour volume is systematically obtained at $X/L_{cav} \approx 0.35/0.4$, for all values of the velocity. These results suggest that a unique curve may be obtained if $\overline{V_{v\,X}}/L_{cav}$ is divided by an appropriate function of U_{ref}.

This point is confirmed in figure 14(a), which shows the evolution of $\overline{V_{v\,X}}/(L_{cav}U_{ref}^{0.6})$ for the different values of U_{ref} at incidences 3°1′, 4°7′, and 5°9. For each angle of attack, all data fit a single curve, which is indicated on the graph as a dotted line. The data are scattered over a range $\pm 5\,\%$ around the curve, which is smaller than the measurement uncertainty. A noticeable influence of the incidence on the vapour volume can be observed in figure 14(a): the shape of the curves remains identical, but the maximum vapour volume increases with the incidence. In figure 14(b), $\overline{V_{v\,X}}/(L_{cav}U_{ref}^{0.6}\alpha_i^{0.4})$ is plotted as a function of X/L_{cav}, for all velocities and all angles of attack. The data

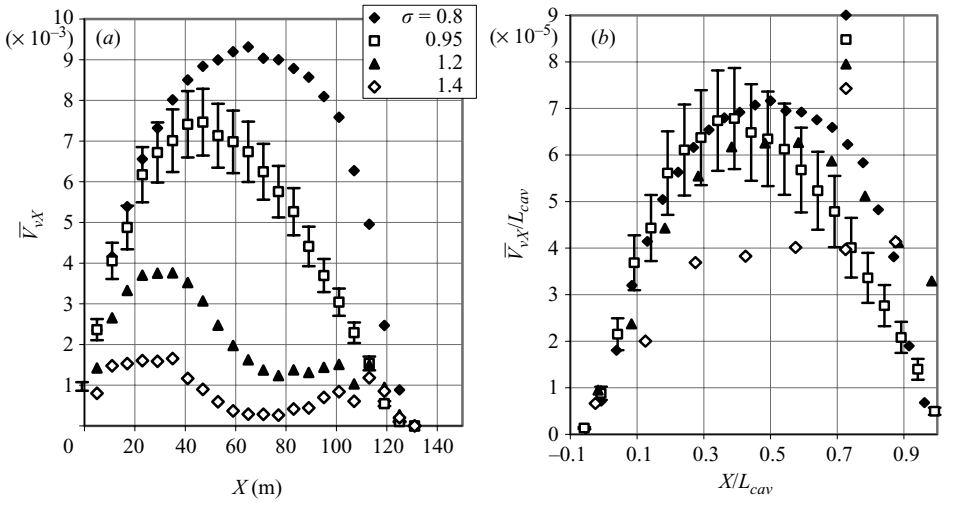

FIGURE 15. Evolution of the vapour volume from the leading edge to the trailing edge. Comparison between cavities of different sizes (measurement set 2, $\alpha_i = 4°7'$, $U_{ref} = 6\,\mathrm{m\ s^{-1}}$).

points are close to a unique curve the equation of which is

$$\overline{V_{v\,X}}\big/\left(L_{cav}\,U_{ref}^{0.6}\alpha_i^{0.4}\right) = a(X/L_{cav})^3 + b(X/L_{cav})^2 + c(X/L_{cav}) + d,$$

with $a = 4.2 \times 10^{-5}$, $b = -10^{-4}$, $c = 6 \times 10^{-5}$, and $d = 2.8 \times 10^{-6}$. This result suggests that for the present foil geometry and sheet cavities of similar lengths, no major change in the two-phase flow structure is obtained, when the velocity or incidence is modified. Of course this conclusion is not valid for cavities of different lengths, as can be seen in figure 15(*a*): the evolution of $\overline{V_{v\,X}}$ is drawn for several cavity lengths $L_{cav}/L_{ref} = 0.25$, 0.4, 0.8, and 0.9. It can be observed (figure 15*b*) that plotting $\overline{V_{v\,X}}/L_{cav}$ as a function of X/L_{cav} does not lead to a single curve: the four cavities are characterized by different two-phase structures.

The evolution of $\overline{V_{v\,Y}}(Y)$ from the foil wall up to the top of the cavity is shown in figure 16 for all incidences and all velocities. As previously, $\overline{V_{v\,Y}}$ at position Y corresponds to the time-average vapour volume in a horizontal plane located at altitude Y, per unit width and depth. In the present case, $\overline{V_{v\,Y}}/(L_{cav}U_{ref}^{0.6})$ is drawn with respect to Y. It can be noticed that the maximum value of $\overline{V_{v\,Y}}/(L_{cav}U_{ref}^{0.6})$ is systematically obtained for Y close to $18\,\mathrm{mm} \pm 2\,\mathrm{mm}$, i.e. nearly at mid-height of the sheet cavity. This was expected, since the variation of α_i between $3°1'$ and $5°9'$ leads to small modifications ($\pm 3\,\mathrm{mm}$) of Y at the foil leading and trailing edges. Moreover, for all angles of attacks and all values of U_{ref}, similar values of $\overline{V_{v\,Y}}/(L_{cav}U_{ref}^{0.6})$ are obtained at mid-height. This is consistent with figure 12(*a*), since it confirms that the maximum void fraction is nearly independent of α_i. Aside from this mid-height point, a significant disparity can be observed: the void fraction increases with incidence. This is consistent with figure 12(*b*), which indicated that $\overline{V_v}$ increases with α_i.

A comparison between the experimental data and the numerical results is given in figure 17. For the three values of the incidence, the evolution of $\overline{V_{v\,X}}/(L_{cav}U_{ref}^{0.6})$ is shown as a function of X/L_{cav} and $\overline{V_{v\,Y}}/(L_{cav}U_{ref}^{0.6})$ as a function of Y. The charts related to the numerical simulations are obtained by averaging the results over $50t/T_{ref}$, i.e. more than 10 oscillations of the sheet cavity. A fair agreement can be observed

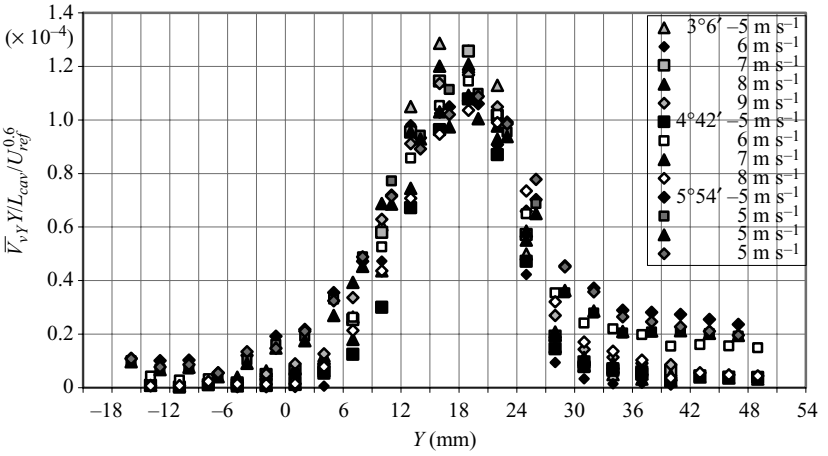

FIGURE 16. Evolution of the vapour volume from the bottom to the top of the cavity. Incidences 3°1′, 4°7′, and 5°9′ (measurement set 2).

concerning the orders of magnitude of $\overline{V_{vX}}$ and $\overline{V_{vY}}$, as well as their evolution through the cavity. It confirms that the time-averaged solution of the numerical simulations is systematically close to the experiments, for α_i varying between 3° and 6°.

5.2. *Flow unsteadiness*

Most of the sheet cavities, even very small, exhibit an unsteady self-oscillatory behaviour for the three angles of attack considered. This unsteadiness is not systematically visible to the naked eye, since the frequency increases up to about 70 Hz in low cavitating conditions. However, it is detected by the analysis of the experimental pressure signal given by the piezo-electric transducer. The self-oscillation cycle has been depicted in detail by Pham *et al.* (1999) in similar conditions with a 4° angle of attack: It mainly consists of three steps: (i) growth of the leading edge cavity with no significant perturbation, (ii) progression of the re-entrant jet close to the foil and perturbation of the interface, (iii) partial cavity break-off when the reverse flow reaches the leading edge, and convection of the cloud of vapour downstream.

Apart from this typical cloud cavitation, steady sheet cavitation is obtained experimentally only in the case of the 3°1 angle of attack, when the cavity is shorter than 3 cm. For such flow conditions no characteristic frequency is detected by the pressure transducer.

For all other conditions, the experimental data obtained from measurement set 1 are reported in figure 18: the Strouhal number (non-dimensional frequency $St = f L_{cav}/U_{ref}$) is plotted as a function of σ/α_i. An almost constant Strouhal number $St = 0.25 \pm 0.03$ is obtained, except in three cases corresponding to very large sheet cavities ($L_{cav}/L_{ref} > 0.9$) respectively at incidence 3°1′, 4°7′ and 5°9′. In these cases, *St* falls in the range 0.11–0.13. The value 0.25 is very close to the one reported by other authors in various configurations of cloud cavitation (Joussellin *et al.* 1991; Le *et al.* 1993; Stutz & Reboud 1997*b*, Pham *et al.* 1999), whereas the lower one is similar to the normalized frequency $St_{\mathrm{ref}} = f L_{ref}/U_{ref} \approx 0.1$ obtained theoretically by Watanabe, Tsujimoto & Furukawa (2001) in the case of very large sheets of cavitation. These authors distinguish 'partial cavity oscillations', corresponding to cloud cavitation with $L_{cav}/L_{ref} < 0.75$, from 'transitional cavity oscillations', occurring for sheets of

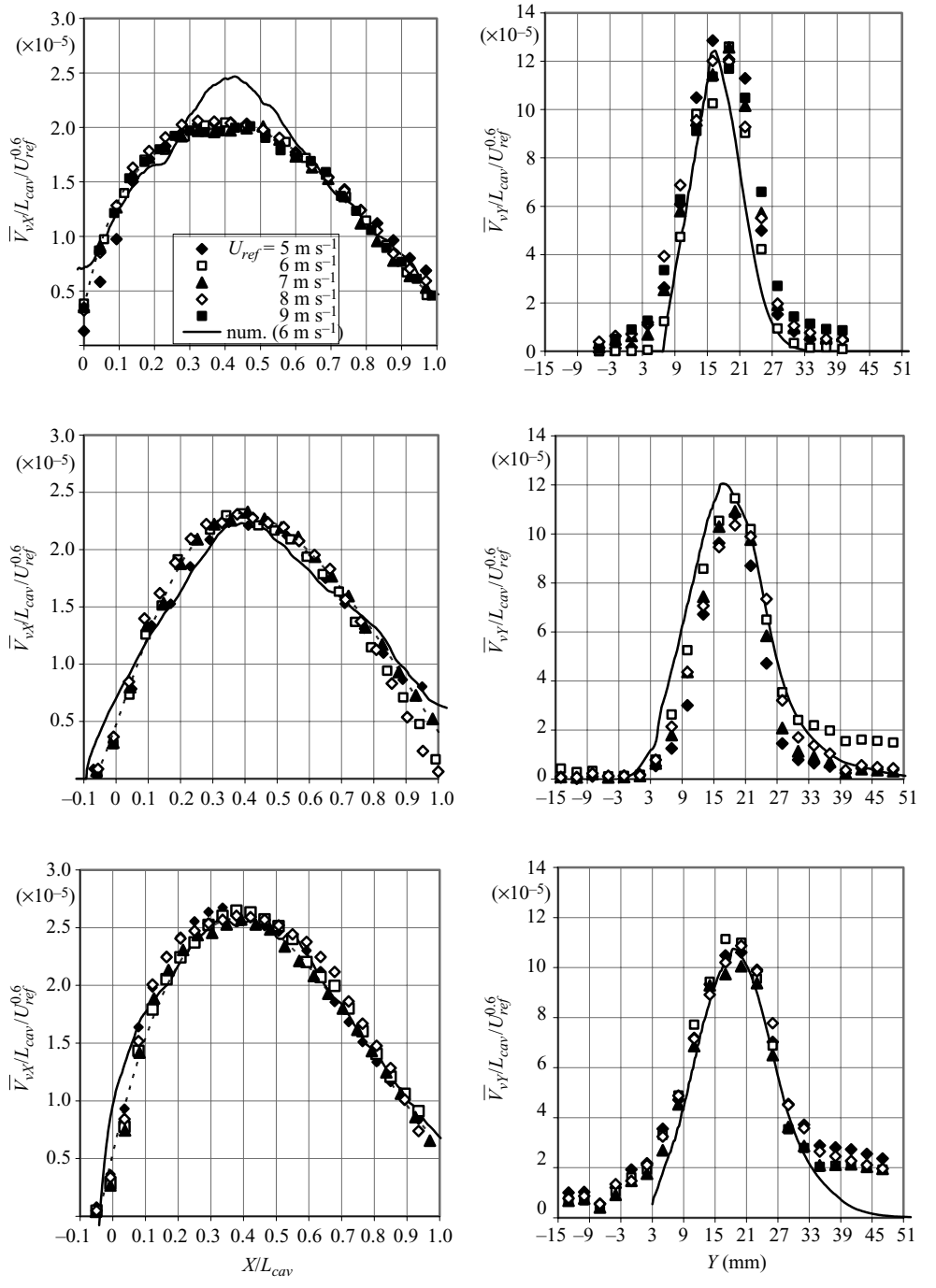

FIGURE 17. Evolution of the vapour volume along X and Y axes. From top to bottom: incidences 3°1′, 4°7′, and 5°9′ Comparison between the experimental data (measurement set 2) and the numerical simulations.

cavitation larger than 75 % of the chord and characterized by a lower Strouhal number. These names will be used hereafter in the present work to differentiate the two results.

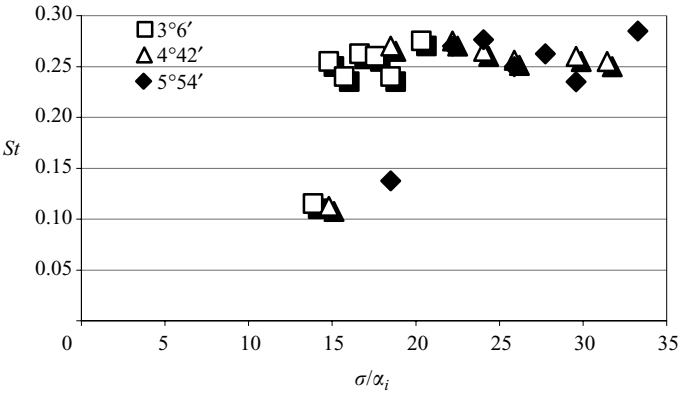

FIGURE 18. *St* as a function of σ/α_i (experiments, measurement set 1).

Numerical simulations also exhibit unsteady cavitating behaviours in all the range of cavitation numbers, excepted for very small sheet cavities at incidence 3°1′, which is consistent with experiments. The frequency of the oscillations can be estimated from the calculated pressure fluctuations upstream of the foil, at the location of the pressure transducer in the cavitation tunnel. Comparisons of the experimental and numerical results are presented in figure 19 for the three angles of attack and the complete range of cavitation numbers considered: the frequency f of the oscillations is plotted as a function of U_{ref}/L_{cav}. Only partial oscillations are considered here ($L_{cav}/L_{ref} \leqslant 0.9$), whereas transitional cavity oscillations will be discussed later. A systematically good agreement is obtained between the experiments and the simulations. The only significant discrepancy concerns the very small cavities at incidence 5°9. However, the visual estimation of the mean cavity length is not precise for such small cavities. The relatively high value of the Strouhal number in this case ($St = 0.29$) as well as the discrepancy with the numerical result could be to some extent related to this uncertainty.

The influence of both velocity and incidence on the cavitation cycle is analysed in figure 20. A nearly constant cavity length $L_{cav}/L_{ref} \approx 0.75$ is maintained at incidences 3°1′, 4°7′ and 5°9′ by varying the cavitation number from 0.7 up to 1.15 (measurement set 2). In these cavitation conditions, velocity is increased from $5\,\mathrm{m\,s^{-1}}$ up to $9\,\mathrm{m\,s^{-1}}$ at incidence 3°1′, and from $5\,\mathrm{m\,s^{-1}}$ up to $8\,\mathrm{m\,s^{-1}}$ at incidences 4°7′ and 5°9′. The evolution of $\overline{\beta}_{\max}$ (maximum value of $\overline{\beta}$ in the flow) confirms the conclusions drawn in § 5.1: no significant effect of the incidence is obtained, and at a given velocity, the values remain close to each other, with discrepancies lower than 10 %. The case $U_{ref} = 5\,\mathrm{m\,s^{-1}}$ and incidence 4°7′ should be considered with caution, since a small imprecision in the cavity length may have a notable effect on the maximum volume fraction of vapour. The velocity increase also has a strong influence on this parameter: its increase can be estimated as about 25 % higher when velocity is increased from $5\,\mathrm{m\,s^{-1}}$ to $9\,\mathrm{m\,s^{-1}}$.

The three other results in figure 20 are derived from the pressure signal analysis. The magnitude of the main frequency peak considerably increases with both incidence and velocity, which indicates a more regular and strong cavitation cycle. This confirms the visual observations during the experiments: noise and vibrations progressively increase when velocity or incidence is increased. At incidence 3°1′ and low velocity, the main frequency peak becomes hardly detectable because its magnitude is very

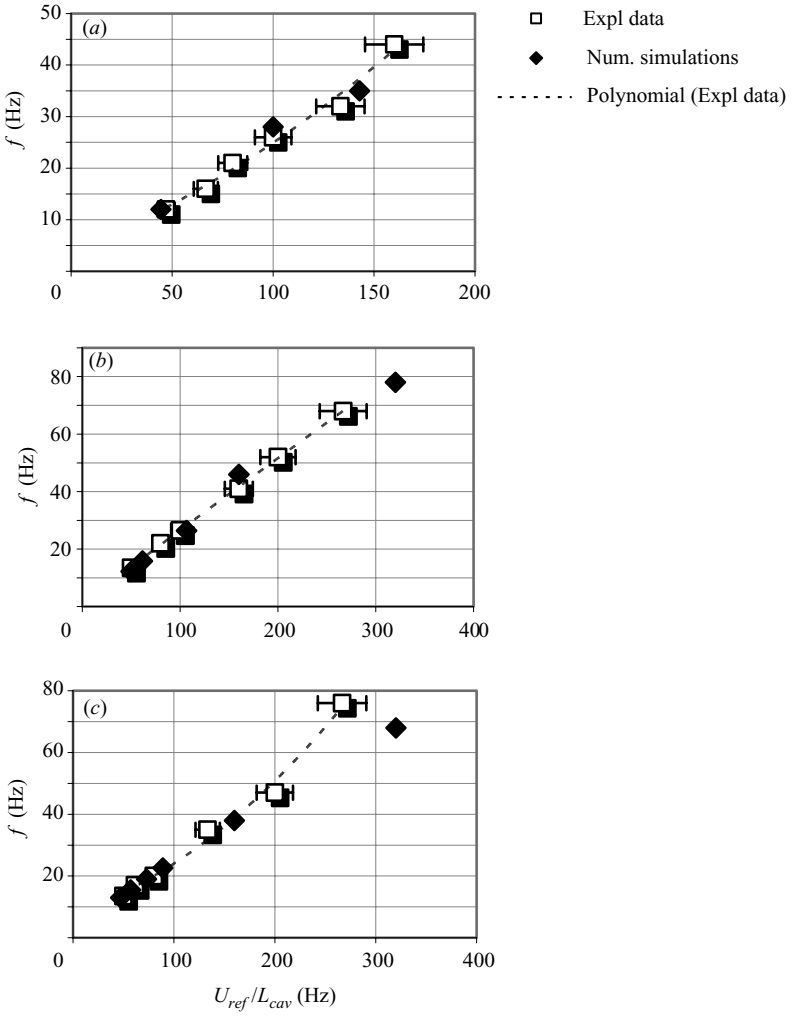

FIGURE 19. Frequency of the cavity self-oscillations (measurement set 1). Comparison between numerical predictions and experimental data for (*a*) incidence 3°1′, (*b*) incidence 4°7′, (*c*) incidence 5°9′.

low. Incidence has almost no influence on the shedding frequency, whereas a velocity increase results in a noteworthy frequency increase. However, the Strouhal numbers decrease from about 0.27 down to 0.24 when U_{ref} is increased from $5\,\mathrm{m\,s^{-1}}$ up to $8\,\mathrm{m\,s^{-1}}$, because the ratio f/U_{ref} decreases. In the present case this frequency modification is not due, as is usual, to a growth of the sheet cavity, since this is maintained constant. Indeed, the increase of the maximum volume fraction of vapour with velocity suggests that the increase of the vapour volume inside the cavitation sheet may be responsible here for the Strouhal number decrease.

Figures 21 and 22 present comparisons between the shedding process predicted by the numerical simulation and that derived from X-ray measurements. Attention is focused first on the details of two cycles in the case of a 3°1′ angle of attack, $U_{ref} = 6\,\mathrm{m\,s}$, and $L_{cav}/L_{ref} = 0.75$. The two illustrations figure 21(*b*, *c*) present the time evolutions of the maximum value of β in each cross-section of the cavitation tunnel,

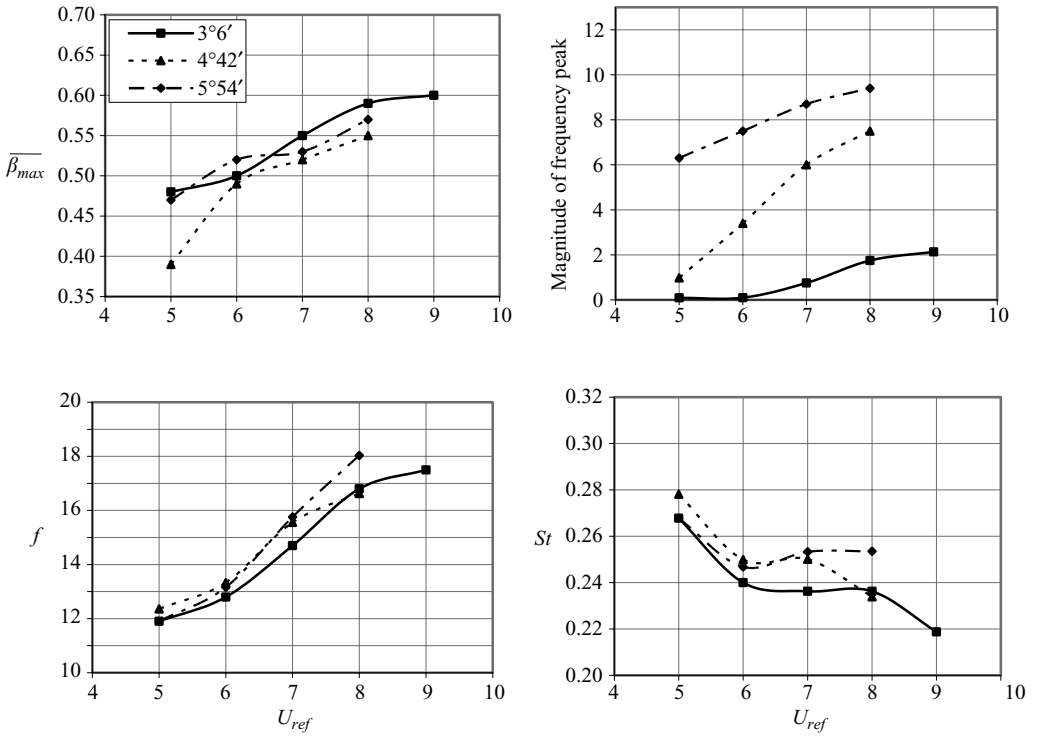

FIGURE 20. Influence of flow velocity and incidence on cavitation at constant cavity length $L_{cav}/L_{ref} \approx 0.75$ (incidence 3°1′: $\sigma = 0.7$, incidence 4°7′: $\sigma = 1$, incidence 5°9′: $\sigma = 1.15$).

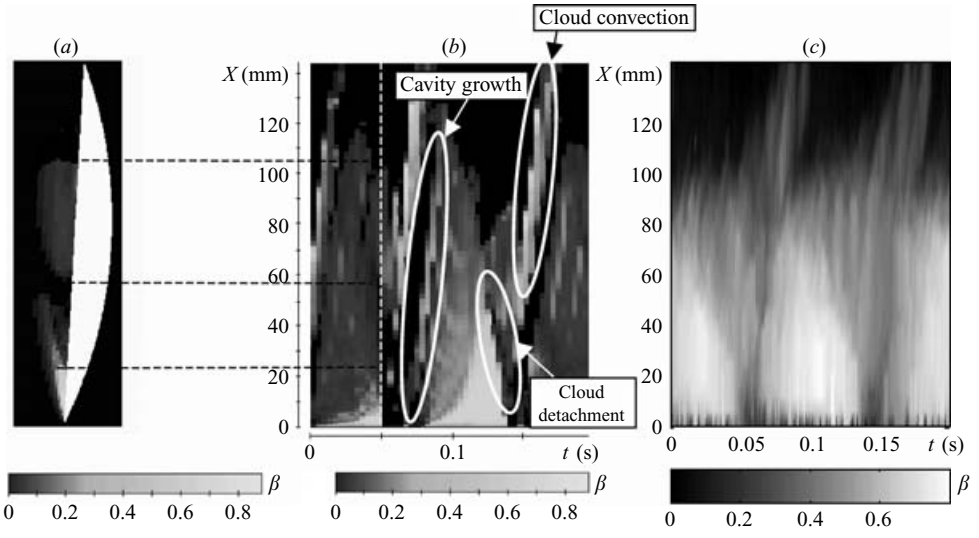

FIGURE 21. Evolution of the cavity during one cycle: comparison between the simulation and the experiments (incidence 3°1′, $U_{ref} = 6\ \mathrm{m\ s^{-1}}$, $L_{cav}/L_{ref} \approx 0.75$). (*a*) Shape and composition of the cavity at time $t = 0.05$ s (calculation). (*b*) Time evolution of β inside the cavity during 1 cycle (simulation). For each position X reported on the ordinate and each time t given on the abscissa, the greyscale indicates the maximum void fraction in the cross-section located at X. The dashed lines indicate the correspondence with (*a*). (*c*) Time evolution of β inside the cavity during 1 cycle (experiments).

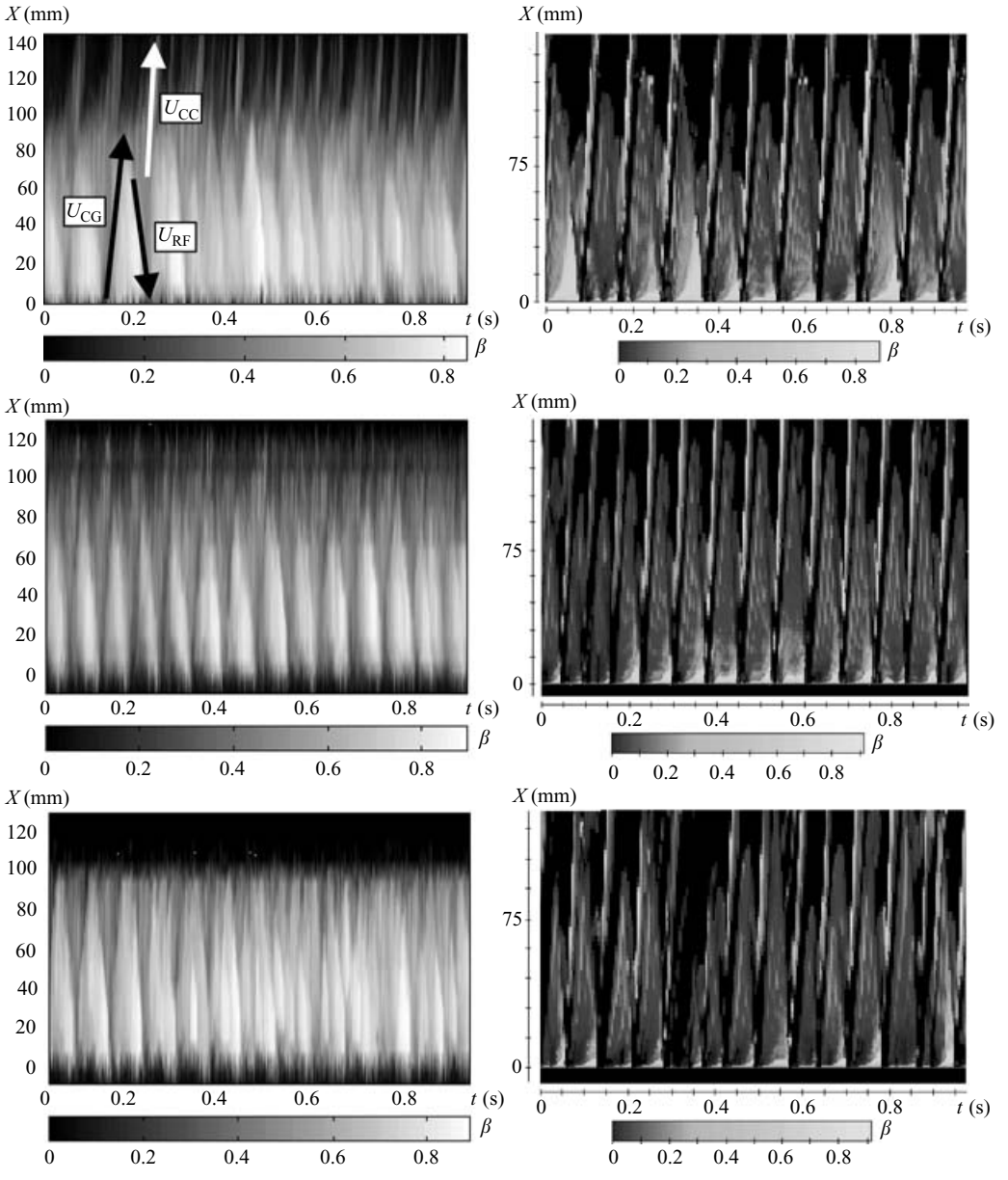

FIGURE 22. Time evolution of the volume fraction of vapour inside the cavity during 1 s ($U_{ref} = 6\,\mathrm{m\,s^{-1}}$, $L_{cav}/L_{ref} \approx 0.75$) (*a*) experiments, (*b*) simulations. From top to bottom: incidences 3°1′, 4°7′, and 5°9′.

from the foil leading edge to trailing edge. The first corresponds to the numerical simulation, while the second is derived from the measurements. Figure 21(*a*) shows an example of the numerically predicted flow configuration for $t = 0.05\,\mathrm{s}$. A fair general agreement is obtained between the two results: the cavity growth, the vapour cloud detachment, and its convection downstream are all predicted by the model. However, significant discrepancies can be observed concerning the magnitude of β: it is underestimated by the model during the cavity growth, and overestimated in the

vapour cloud after its detachment. Note that this second point may be due to the space averaging because of the size of the volume measurements in the experiments: higher local volume fractions of vapour may be detected with smaller detectors. Three-dimensional effects may also partially explain these discrepancies: recall that results obtained by X-ray absorption are averaged in the spanwise direction, so effects of the boundary layers on the sidewalls are included in the values of β. Thus, it is expected that two-dimensional calculations should be able to reproduce the main mechanisms of the sheet cavity dynamics, whereas subtle features of the flow, such as local instantaneous values of vapour volume fraction, may be in imperfect agreement with the X-ray measurements.

After the end of the cavity growth, the experimental results exhibit a progressive splitting of the sheet cavity, which starts downstream and then propagates upstream. The volume fraction of vapour β downstream from the split decreases significantly. When the perturbation is almost 20 mm from the foil leading edge, all the cavity clearly detaches and starts to move downstream. This suggests that the cavity break-off is not directly due to the fact that the re-entrant jet reaches its upstream end and cuts the interface: it may be also associated with the strong modification of the cavity composition during the reverse flow progression.

This process, i.e. the upstream propagation and the modification of the β distribution, is predicted well by the numerical model. Discrepancies mainly affect the rear part of the cavity, where the flow is assumed to completely condense during the re-entrant jet progression, which is not the case in the experiment. A slight difference can also be observed at the cavity inception point, which is fluctuating experimentally, whereas it remains completely stable in the calculation. However, the main process characteristics, such as the progressive decrease of β during the reverse flow propagation, are satisfactorily simulated. This fair agreement is confirmed in figure 22, which displays the comparison between the experimental and the numerical results during a longer time interval of 1 s, for the three angles of attack. The predicted shedding frequency is generally systematically in reliable agreement with the measured one. However, significant disagreements can be observed at incidence $4°7'$: in the experiment, vapour shedding seems to be composed of successive small detachments, while in the simulation only a large cloud of vapour is obtained. As previously mentioned, measurements in the cavity wake are not available at $5°9'$, but the same discrepancy is expected.

The influence of both reference velocity and foil incidence on the characteristics of the cavitation cycle is investigated in figure 23 on the basis of the experimental measurements. The velocity of cavity growth, the progress of the perturbation from the cavity downstream end, and cloud convection are indicated as functions of the reference velocity U_{ref} (see also the three arrows in figure 22 to illustrate these three velocities). Velocities derived from the numerical results are also indicated for the single case $U_{ref} = 6\,\mathrm{m\,s^{-1}}$. Both experimental and numerical velocities were obtained by analysing 20 cycles and then averaging the values. The standard deviation is every time in the range 0.05–0.1 $\mathrm{m\,s^{-1}}$, which gives an indication of the precision of the results.

The cavity growth velocity U_{CG} only slightly changes when incidence is changed, whereas it increases nearly linearly with U_{ref}. All the velocities follow closely to the relation $U_{CG} = U_{ref}/2$, which is consistent with the value of $2.4\,\mathrm{m\,s^{-1}}$ reported recently by Leroux *et al.* (2005) for a NACA66 foil section configuration with $U_{ref} = 5.33\,\mathrm{m\,s^{-1}}$. This indicates that the flow inertia is not the only dominant effect in the vaporization process. The cloud convection velocity U_{CC} is much closer to U_{ref}. In fact, U_{CC} is

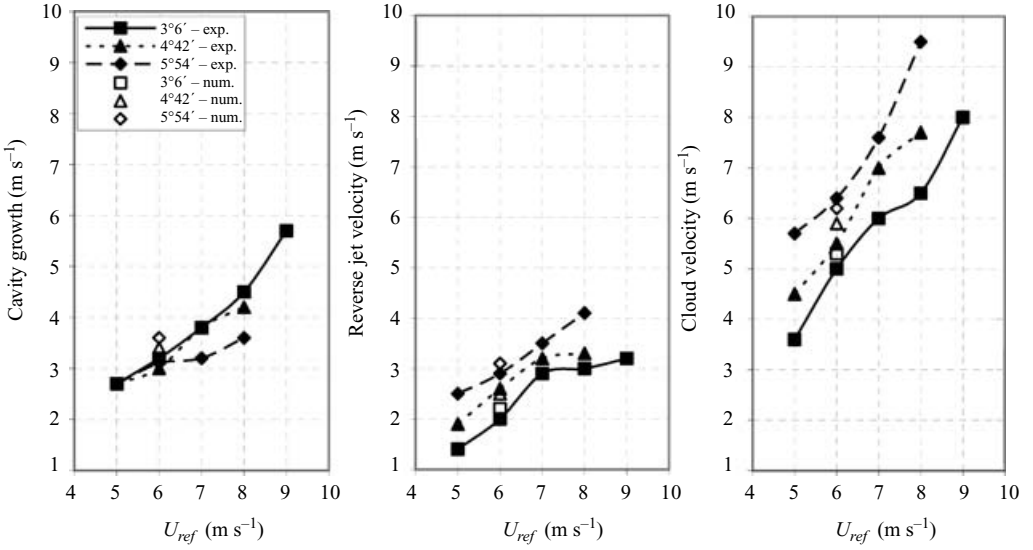

FIGURE 23. Mean velocity of cavity growth, re-entrant jet, and vapour cloud convection, as functions of the inlet flow velocity.

nearly identical to U_{ref} at incidence 4°7′, while it is slightly lower at incidence 3°1′ and slightly higher at incidence 5°9′. This result shows that between the cloud detachment and its final collapse, the cloud motion is a simple convection by the main stream. It also suggests that phase changes are not significant during this motion. The increase of the cloud velocity with incidence could be related to the increase of the obstruction generated by the foil and the cavitation sheet in the test section, which leads to higher velocities outside from the cavity.

The reverse flow velocity U_{RF} is of the same order of magnitude as U_{CG}. However, it is systematically slightly smaller, close to the relation $U_{RF} = U_{ref}/2.5$. The influence of the incidence is more distinct than for U_{CG}: U_{RF} is nearly 1 m s^{-1} higher at 5°9′ than at 3°1. For the three velocities U_{CG}, U_{CC} and U_{RF}, a fair agreement between experiments and simulations is obtained: discrepancies never exceed 0.5 m s^{-1}. The reverse flow velocity is particularly close to the experimental data at all incidences, which confirms that the main mechanisms of its progress are predicted well by the model.

When a 60 % increase is applied to U_{ref} (from 5 m s^{-1} up to 8 m s^{-1}), the same order of magnitude is obtained for the increase of U_{CG}, U_{CC}, and U_{RF}, since these velocities were found to be all nearly proportional to U_{ref}. However, only a 40 % increase of the shedding frequency f is measured at the same time (see figure 20). This indicates that the vapour shedding is not governed only by the cavity growth, the reverse flow progress, and the cloud convection. The frequency may also depend on a fourth mechanism, such as the cloud collapse. The cloud collapse duration may be nearly independent of U_{ref}, which would explain why the frequency does not increase proportionally to the flow velocity. It was previously found by Leroux *et al.* (2005) that the collapse may have a strong influence on the cavitation cycle, because of a pressure wave propagating from the collapse location towards the cavity. In some situations the high intensity of the pressure wave was found to be responsible for a temporary stopping of the next cavity growth, resulting in a drastic reduction of the cycle frequency. The present results also suggest an interaction between the cloud collapse and the next cavity evolution. This point will be investigated in § 6.

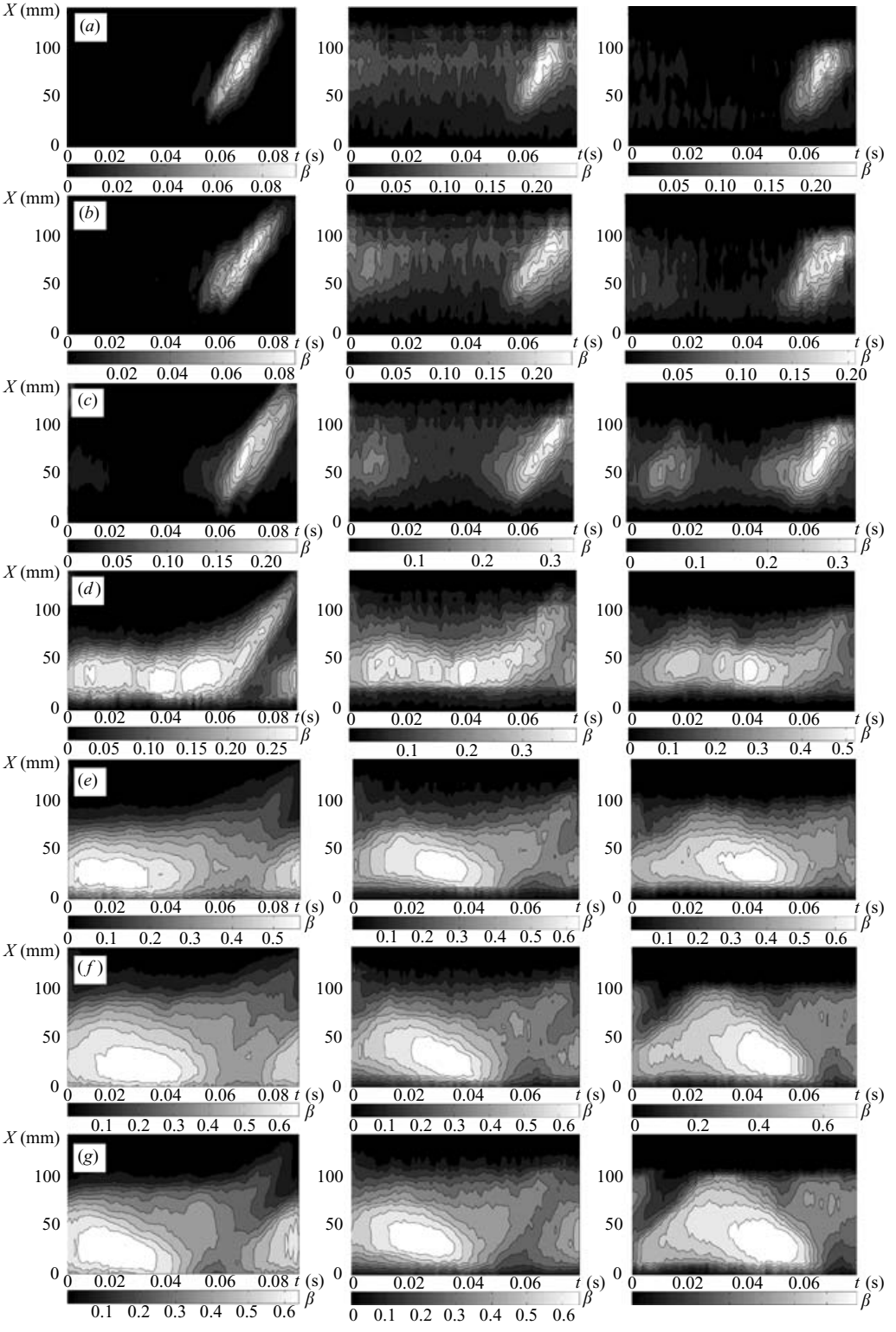

FIGURE 24. For legend see facing page.

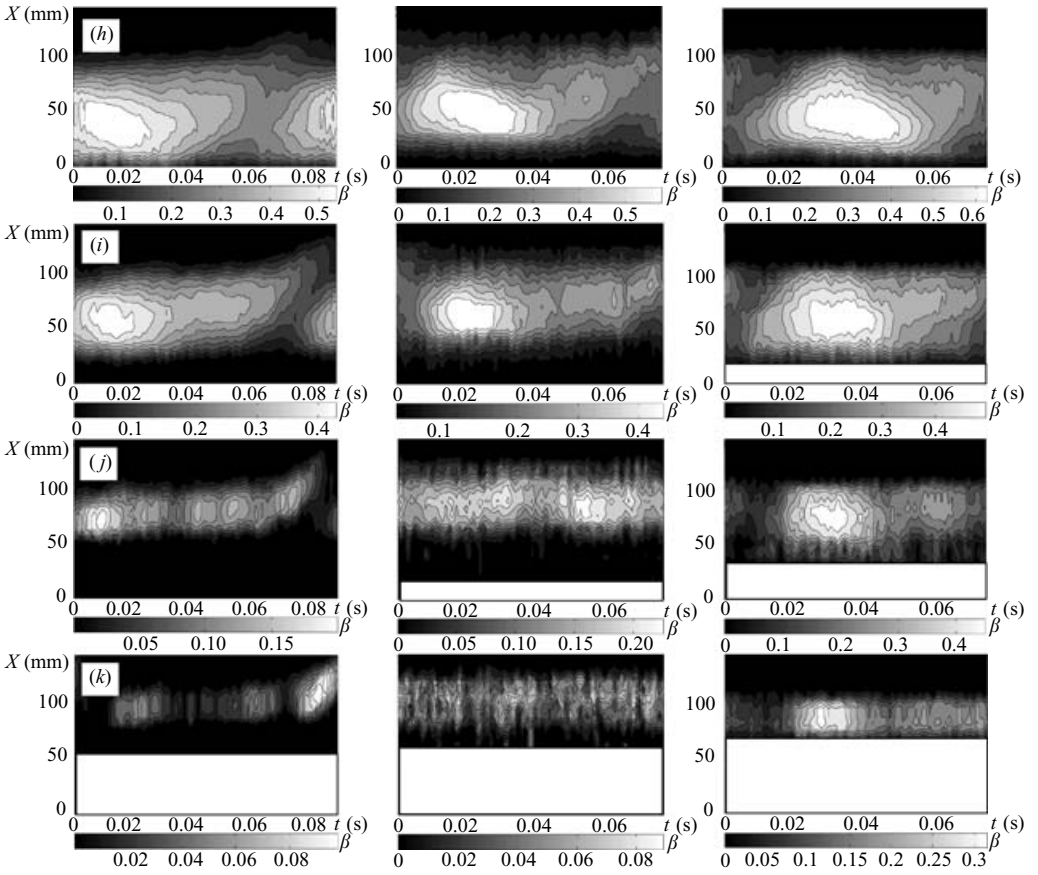

FIGURE 24. Time evolution of the phase-average volume fraction of the vapour phase ($U_{ref} = 6\,\mathrm{m\,s^{-1}}$, $L_{cav}/L_{ref} \approx 0.75$). From left to right: incidences 3°1′, 4°7′, and 5°9′. From top to bottom: height 38 mm down to height 8 mm. Areas located inside the foil are coloured white.

Figure 24 presents the evolution of the phase-averaged volume fraction of vapour. The flow conditions still are $U_{ref} = 6\,\mathrm{m\,s^{-1}}$ and $L_{cav}/L_{ref} \approx 0.75$. From left to right, pictures correspond to incidences 3°1′, 4°7′, and 5°9′, respectively. Each picture presents the evolution of the phase-averaged volume fraction β from the foil leading edge to its trailing edge during one period, i.e. nearly 0.081 s at incidence 3°1′, and 0.076 s at both other incidences. The first line (a) of pictures corresponds to the detectors located at height 38 mm, while the last one (k) corresponds to height 8 mm. It was previously mentioned in § 3 that the vertical size of the volume crossed by X-rays is 3 mm (in the middle of the test section). So results corresponding to eleven successive heights are given here. Note that the lowest heights partially cross the hydrofoil: the areas located inside the foil are shown in white on the pictures. Twenty successive cycles are used for the phase averaging method, and the end of the cloud collapse was chosen as a reference for the end of the period at all incidences.

Lines (a) to (c) correspond to heights where only cloud convection is detected. The attached cavity is located lower, between heights (d) and (k). Line (h) nearly corresponds to the foil leading edge position, so results presented between (i) and (k) do not include the upstream part of the cavity. The successive steps of the cavitation

cycle appear clearly in the pictures. For example in the case of incidence 3°1′, the cavity growth occurs for $0 < t < 0.02$ s, then the progressive transformation of its composition during the re-entrant jet development is observed between $t \approx 0.02$ and 0.04 s. The vapour cloud detachment, detected by a motion at the downstream end of the cavity (see for example line *d*), starts at $t \approx 0.05$ s, and its convection continues until it collapses at $t \approx 0.08$ (see line *a*). This flow evolution is modified when incidence is increased: at 5°9′, a significant time interval is observed between the vapour cloud collapse ($t \approx 0.08$ s) and the growth of the next cavity, which starts only at $t \approx 0.01$ s. This time interval is close to zero at incidence 4°7′, while at 3°1′ the next cavity growth has started before the end of the collapse. This confirms that the cloud implosion plays a major role in the cavitation cycle.

Detailed information concerning the maximum volume fraction of vapour is given in figure 24. Highest values are obtained at height 23 mm (line *f*) at the end of the cavity growth, i.e. at $t \approx 0.02$ ($\beta = 0.64$), 0.025 ($\beta = 0.67$), and 0.045 ($\beta = 0.71$) for incidences 3°1′, 4°7′, and 5°9′, respectively. A slight effect of incidence is thus observed, which was not the case with the maximum time-averaged volume fractions $\overline{\beta}_{\max}$ (see figure 12). Figure 24 also confirms that the cavitation sheet structure is strongly modified during the re-entrant jet development: a large reduction of the void fraction is observed from line (*e*) to (*i*) between the end of the cavity growth and the cloud detachment. This indicates that during this time interval the void fraction decreases from 55 %–70 % down to 25 %–35 % over nearly all the cavity height.

Pictures in lines (*c*) and (*d*) exhibit some fluctuations of β at the top of the attached cavitation sheet. Indeed, the maximum void fraction in line (*d*) for $0.01 < t < 0.05$ is oscillating, and some vapour is detected intermittently at height (*c*) at incidences 4°7′ and 5°9′.

6. Analysis of partial and transitional cavity oscillations

In this section the mechanisms that govern the flow instability in partial cavity oscillations and transitional cavity oscillations are discussed on the basis of the numerical simulations; the good agreement between experiments and predictions shown previously for both conditions allows us to perform a more detailed investigation of the numerical results.

6.1. *Partial cavity oscillations*

It was reported by Pham *et al.* (1999) that partial cavity oscillations are directly driven by the re-entrant jet that periodically flows under the cavity towards the leading edge. When this reverse flow reaches the cavity upstream end, it cuts the interface. This leads to the splitting of the cavity and the separation of its rear part, which is then convected by the main flow downstream. This phenomenon is illustrated in figure 25, which presents the nine successive shapes of the sheet cavity obtained during a complete cavitation cycle at incidence $\alpha_i = 4°7'$ and $\sigma = 1.32$ (in this case $L_{cav}/L_{ref} \approx 0.4$). The shapes are obtained by phase averaging. The bottom part of each image corresponds to the numerical result, and the upper part to experiments. It can be observed that the evolutions of the cavity shape are similar in the two cases. The calculation correctly predicts the re-entrant jet flowing upstream close to the foil, as reported experimentally by Pham *et al.* (1999) in the same configuration. A small sheet cavitation is also obtained by the numerical model on the foil pressure side, which does not seem to be the case in experiments. However, the very low void fraction predicted by the model in this area (less than 5 %) is difficult to detect

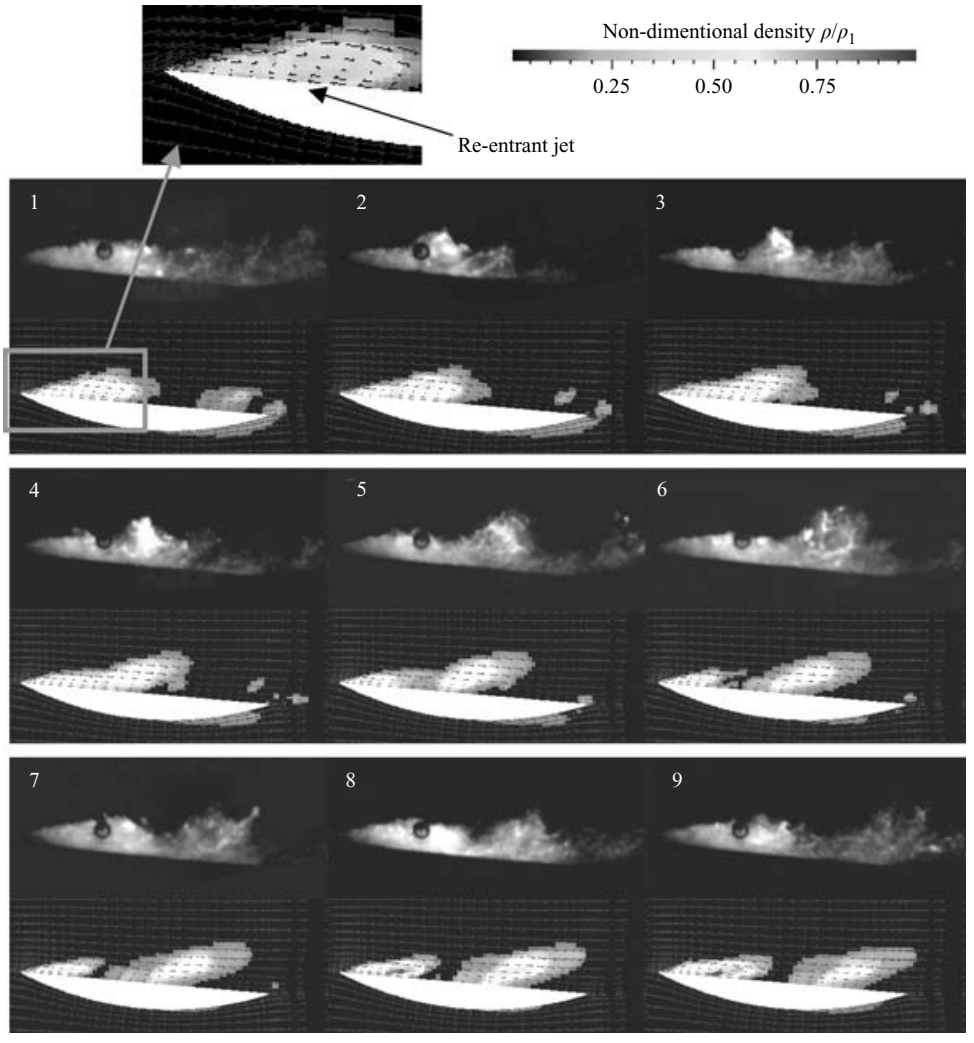

FIGURE 25. Phase-averaged cycle of partial cavity oscillations ($\sigma = 1.32$, angle of attack 4°7′). Top: cavity shape obtained by image processing of experimental side views of the cavity. Bottom: numerical result.

visually. Moreover, even though a pressure close to P_v is obtained on the bottom side of the foil section in the experiments, all the cavitation nucleii may be carried away by the flow, since no recirculation occurs on this side of the foil. In this case, no area of cavitation would be obtained in the experiments, while it would be predicted by the model because of the local low pressure. A small pressure side cavity is observed in the cavitation tunnel for slightly lower pressure conditions.

Figure 26 shows plots of two variables as functions of time in the case of partial cavity oscillations: (*a*) the non-dimensional re-entrant jet velocity u/U_{ref} at station $X/L_{ref} = 0.3$, and (*b*) the pressure coefficient $C_p = (P - P_{\mathrm{ref}})/\frac{1}{2}\rho U_{ref}^2$ at station $X/L_{ref} = 0.5$, which is nearly the point of cavity detachment on the foil surface. P and P_{ref} are the local and outlet static pressures, respectively. It can be checked that the re-entrant jet development is strongly correlated to the detachment of the previous cloud of vapour: its convection downstream results in a significant re-increase of the

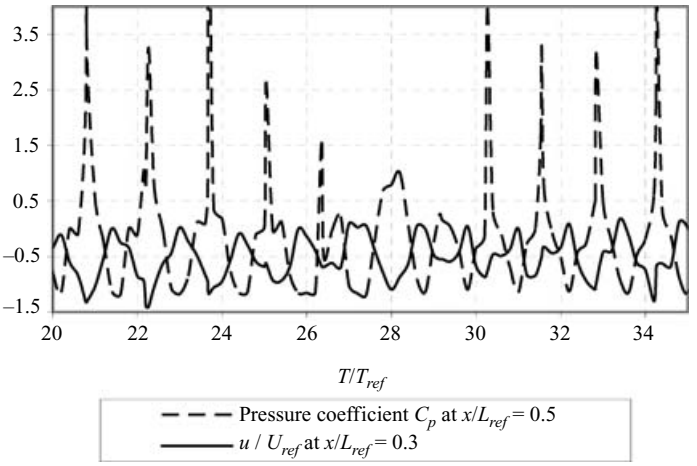

FIGURE 26. Correlation of the pressure increase in the cavity wake with the inception of the re-entrant jet. (Partial cavity oscillations: $\sigma = 1.32$, angle of attack 4°7′).

pressure in the cavity wake, and this local pressure gradient may be responsible for the reversal of the flow from this area to the foil leading edge. This important role played by the adverse pressure gradient in the cavity wake in the development of the re-entrant jet, and thus in the inception of cloud cavitation, was previously described by Laberteaux & Ceccio (2001) and Callenaere *et al.* (2001).

The organization of the periodic cavitation cycle is now investigated in the case of larger cavities ($\sigma = 1.1$, $L_{cav}/L_{ref} \approx 0.7$). Figure 27 shows, for incidences 3°1′, 4°7′, and 5°9′, the successive occurrence of (*a*) the re-entrant inception, (*b*) the cavity break-off, and (*c*) the collapse of the cloud of vapour. The oscillation of the pressure at the point of sheet cavity detachment is also reported, to visualize the evolution of the cycle. This point is now the foil trailing edge, while it was $X/L_{ref} = 0.5$ for previous smaller cavities. It can be observed that no systematic correlation between the inception of the reverse flow and the collapse of the previous cloud of vapour is obtained: sometimes the collapse happens first, sometimes the re-entrant jet starts first. This suggests that the pressure wave generated by the implosion of the vapour cloud plays only a minor role in the flow unsteadiness in the present configuration. This is very different from previous observations reported by Leroux *et al.* (2005) in the case of a NACA foil section. However, in that study, no recirculation was observed on the foil suction side at non-cavitating conditions, while in the present case, a large recirculation, due to the sharp leading edge, is obtained. So, here, the sheet cavity is characterized by very low velocities, and the re-increase of the pressure at the foil trailing edge after the convection of the cloud of vapour is strong enough to generate the re-entrant jet. In the NACA configuration, the re-entrant jet flowed against a strong incoming flow on the foil suction side, so the influence of the pressure wave due to the cloud collapse may be necessary to produce the reverse flow.

The cavity break-off is systematically obtained when the trailing-edge pressure is maximum. This is not surprising, since it may correspond to the maximum intensity of the re-entrant jet. It can be also noted that the delay between the inception of the re-entrant jet and the cavity break-off is almost constant, which suggests that the cloud detachment depends only on the re-entrant jet velocity, with no influence of the pressure wave due to the previous collapse.

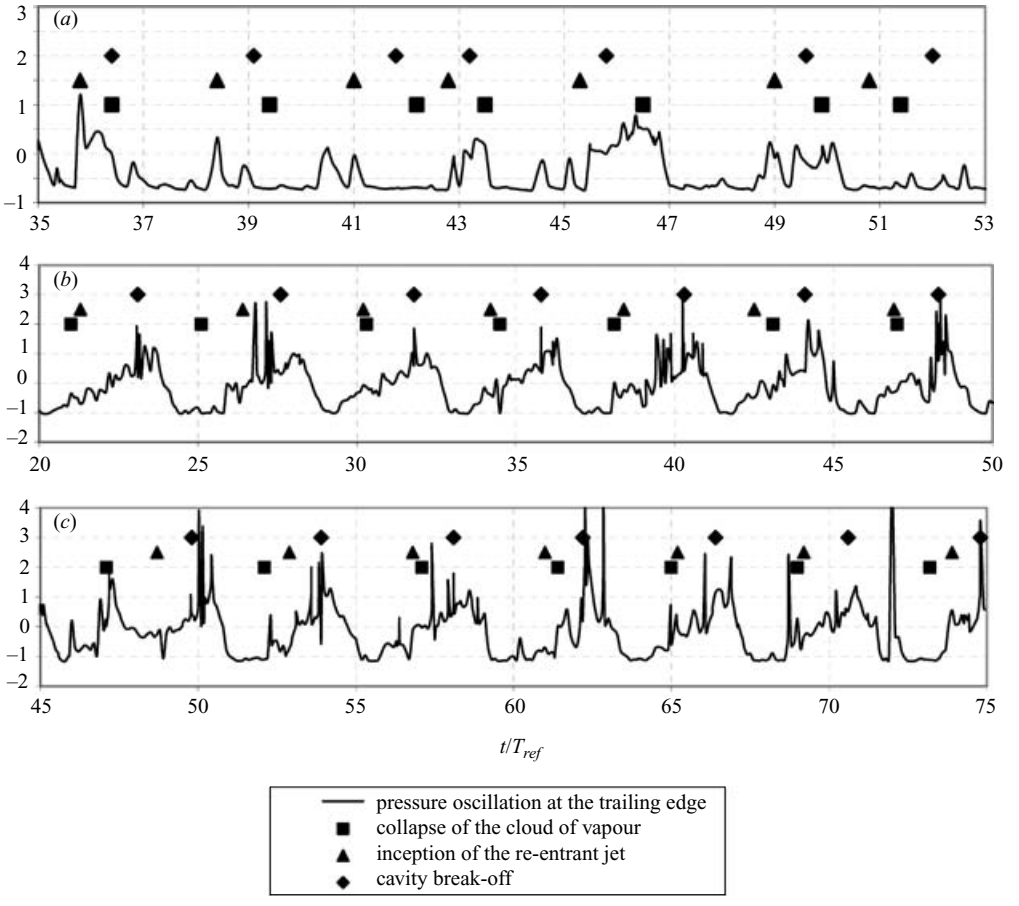

FIGURE 27. Analysis of the cavitation cycle (partial cavity oscillations, $\sigma = 1.1$, $U_{ref} = 6\,\mathrm{m\,s^{-1}}$). (*a*) $\alpha_i = 3°1'$, (*b*) $\alpha_i = 4°7'$, (*c*) $\alpha_i = 5°9'$.

In this case of sheet cavitation ($L_{cav}/L_{ref} \approx 0.7$), a small pressure-side cavity is obtained both in the experiments and in the numerical simulations. A periodical interaction between the sheet cavities on the two sides of the foil section can be observed in the results of the calculations. As shown in figure 28, the growth of the leading-edge cavity does not directly lead to its break-off and the convection of its rear part downstream. A supplementary step consisting of (i) a stabilization of the maximum attached cavity, and (ii) a significant decrease with no break-off, is observed before a second growth and the final detachment of the main part of cavity. However, this modification of the periodic cycle does not modify the vapour shedding frequency, and Strouhal numbers close to 0.25–0.3 are still obtained.

To investigate the interaction between the two sides, an analysis of the cavitation cycle for $\sigma = 1.1$ is now performed, especially during sequence B reported in figure 28 (stagnation and decrease of the cavity with no vapour shedding). Figure 28(*a*) shows the length of the sheet cavity on the suction side (top graph) and pressure side (bottom graph) as a function of time. The sequence of events A, B, and C is indicated and pictures of the cavity for the situations A and B are shown in figures 28(*b*) and 28(*c*) respectively. The main difference with the previous configuration ($L_{cav}/L_{ref} \approx 0.4$) is a strong interaction between pressure- and suction-side sheet cavities. This interaction

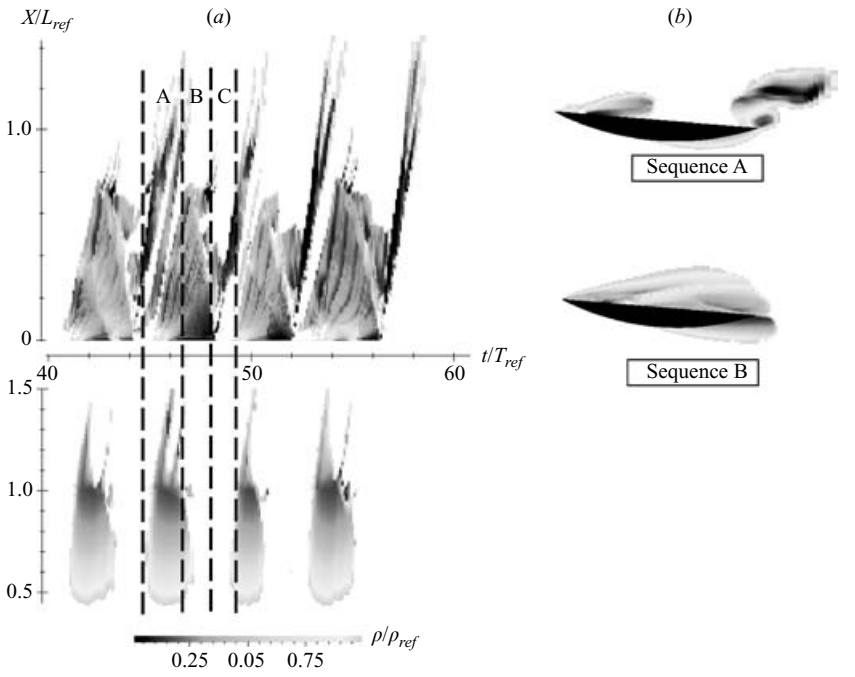

FIGURE 28. Numerical prediction of partial cavity oscillations with interaction at the foil trailing edge (incidence 4°7′, $\sigma = 1.1$). (*a*) Evolution during four cycles of the pressure side cavity (bottom) and the suction side cavity (top). Each cycle is composed of sequences A (cavity growth), B (cavity stagnation and decrease), C (second growth and cloud detachment). (*b*) Sheet cavity illustrating the interaction during sequence A. (*c*) Sheet cavity illustrating the interaction during sequence B.

is characterized by a substantial growth of the pressure-side cavity when a large quantity of vapour reaches the trailing edge on the upper face. This phenomenon can be observed consecutively (i) during the passage of the vapour cloud at the foil trailing edge (sequence A), and (ii) between the end of the sheet cavity growth and its break-off (sequence B).

Figure 29 shows the time evolution during five cycles of (*a*) the pressure coefficient C_p on the foil suction side at the trailing edge, (*b*) the non-dimensional velocity u/U_{ref} of the re-entrant jet at station $X/L_{ref} = 0.7$, and (*c*) the non-dimensional vorticity at the foil trailing edge. Events A, B, and C are indicated on the graphs. The figure reveals that only a weak re-entrant jet is present under the cavity during sequences A and B, i.e. during the pressure/suction side interaction at the trailing edge: u/U_{ref} is close to zero at stations $X/L_{ref} = 0.7$. The reverse flow becomes much stronger just at the beginning of sequence C, after the collapse of the pressure-side cavity. Then it flows upstream during sequence C and finally results in the cavity split at the end of this sequence. The weakness of the re-entrant jet during steps A and B may be due to the very low pressure level imposed at the trailing edge by the pressure-side cavity: the strong adverse pressure gradient that was assumed to be responsible for the jet formation is not obtained in the present case (see the evolution of C_p in figure 29), so the reverse flow remains very slow, simply due to the general recirculation movement in the cavity. As a consequence, no cavity break-off is observed during sequence B. After the decrease of the sheet cavity on the foil pressure side, the sudden increase

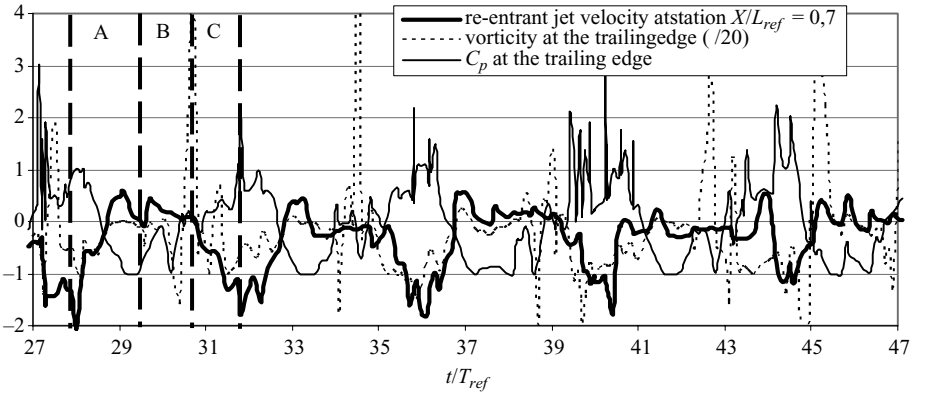

FIGURE 29. Correlation of the pressure increase in the cavity wake with the inception of the re-entrant jet and the increase of the vorticity at the trailing edge. (Partial cavity oscillations: $\sigma = 1.1$, angle of attack 4°7′).

of the pressure at the trailing edge immediately leads to the amplification of the re-entrant jet intensity and the continuation of the standard cycle.

It can also be observed in figure 29 that the inception of the re-entrant jet is correlated with a peak of vorticity at the foil trailing edge. This point is illustrated by figure 30, which shows the evolution of the vorticity field at the trailing edge during the formation of the re-entrant jet. According to this sequence, this jet is generated by a vortex that results from the interaction between the boundary of the cavity and the boundary layer on the foil pressure side.

6.2. *Transitional cavity oscillations*

In the special case of transitional cavity oscillations ($L_{cav}/L_{ref} \geqslant 0.9$) numerical results show two characteristic frequencies: a first one (denoted frequency 1 hereafter), which leads to a Strouhal number close to 0.25–0.3, and a second (frequency 2) equal to half the first one, leading to Strouhal numbers in fair agreement with the experimental measurements for such sheet cavities ($St \approx 0.13$–0.16). Frequency 1 is based on upstream pressure fluctuations, as stated previously, whereas frequency 2 can be detected for example by plotting the time evolution of the pressure just downstream from the foil trailing edge. It can be seen in figure 31 that frequency 1 is consistent with the sheet cavity oscillations on the pressure side, while frequency 2 characterizes the vapour cloud shedding on the suction side. The increase of the delay between two cloud detachments is due to a more complex cavitation cycle than the one described previously for standard partial cavity oscillations. As shown in figure 31(*a*), in the present case the cycle is composed of (i) the growth of the leading-edge cavity (sequence A), (ii) its stagnation due to the pressure-side cavity (sequence B), (iii) the progression of the re-entrant jet and the cavity break-off (sequence C), (iv) the stopping of the cloud of vapour on the foil suction side, with only little vapour shedding downstream (sequence D), and (v) the final convection of the cloud of vapour (sequence E). In comparison with partial cavity oscillations, sequences A, B, C are the same, whereas sequences D and E are new, and are responsible for the low value of frequency 2.

The stopping of the vapour cloud convection during sequence D can be seen rather clearly in figure 31(*a*): the distance between the cloud of vapour and the foil leading edge does not increase, even though some slight vapour shedding can be observed

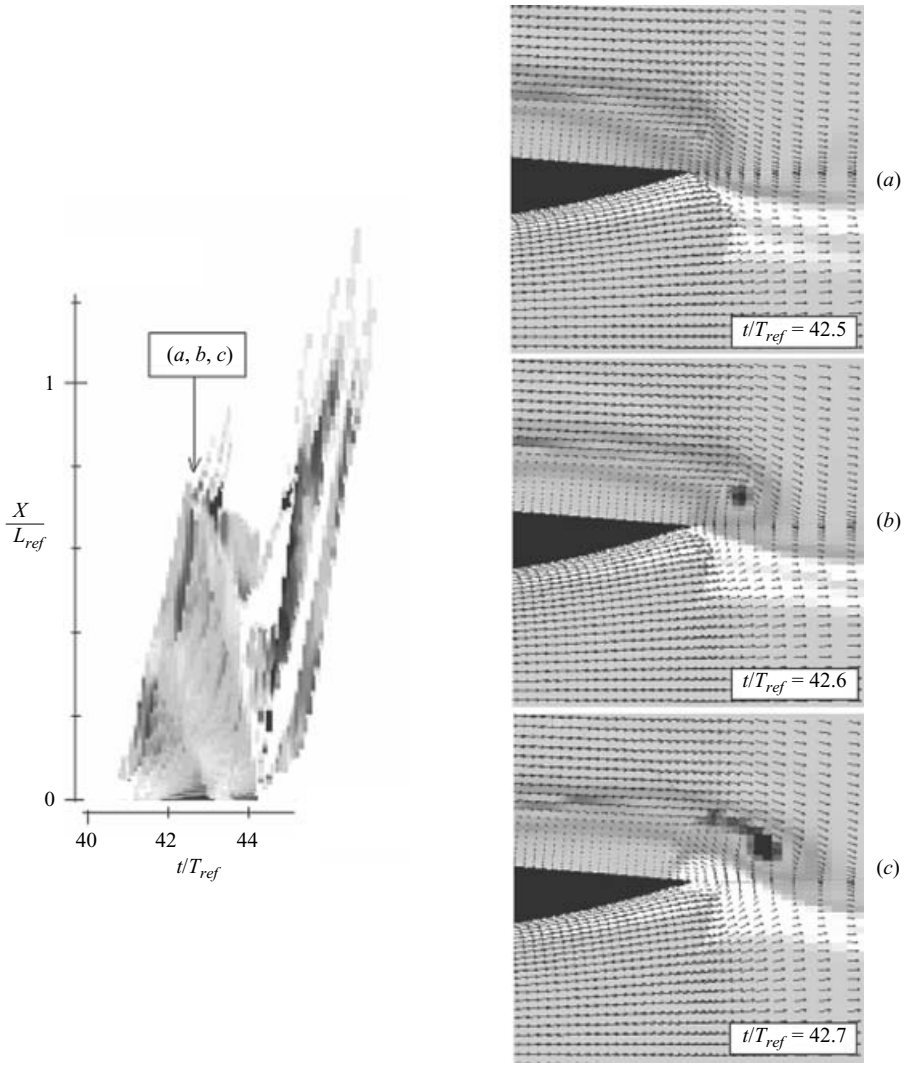

FIGURE 30. Evolution of the vorticity at the trailing edge during the inception of the re-entrant jet. (Partial cavity oscillations: $\sigma = 1.1$, angle of attack $4°7'$).

downstream. This behaviour may be associated with the large pressure-side sheet cavity growing during sequence D: the interaction between both sides of the foil section (see figure 31*b*) seems to block the convection of the cloud, until the pressure-side cavity is removed (figure 31*c*). During this time, the next cavity cannot grow at the foil leading edge, so the next sequence A is delayed. This amplification of the interaction between the pressure and suction sides may be due to the increase of the volume of vapour on both sides: it nearly doubles when σ is reduced from 1.1 to 0.88.

Figure 32 shows the time evolutions of C_p at the leading edge, C_p behind the trailing edge, and the re-entrant jet intensity u/U_{ref} at station $X/L_{ref} = 0.5$. Frequencies 1 and 2 can be observed in the pressure signals. It can be noticed that during sequence E, u/U_{ref} becomes positive, because of the convection of the cloud, so no re-entrant

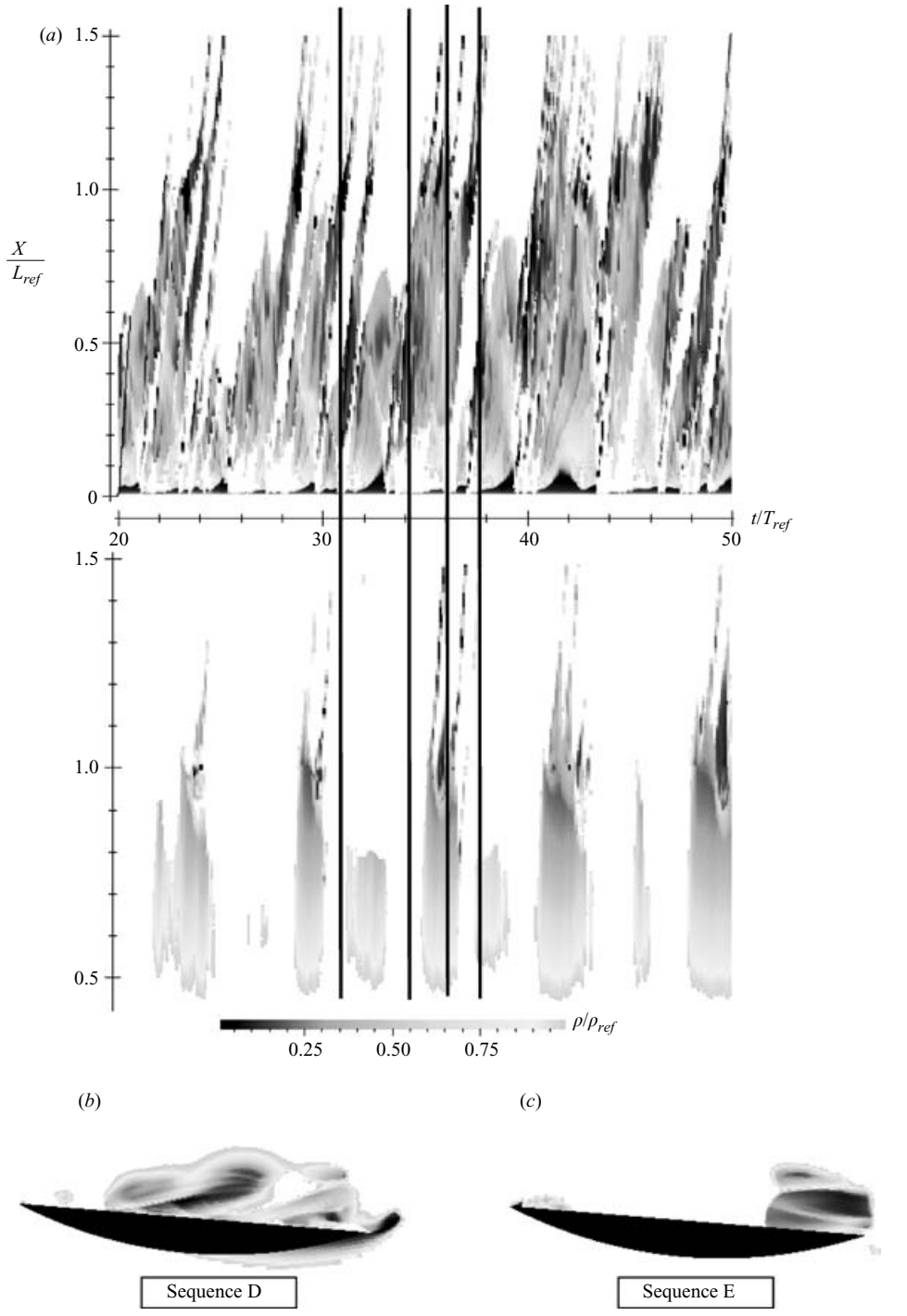

FIGURE 31. Interaction at the foil trailing edge (transitional cavity oscillations: $\sigma = 0.88$, angle of attack 4°7′). (*a*) Evolution of the cavity length on the pressure side (bottom) and the suction side (top). (*b*) Sheet cavity illustrating the interaction during sequence D. (*c*) Sheet cavity illustrating the interaction during sequence E.

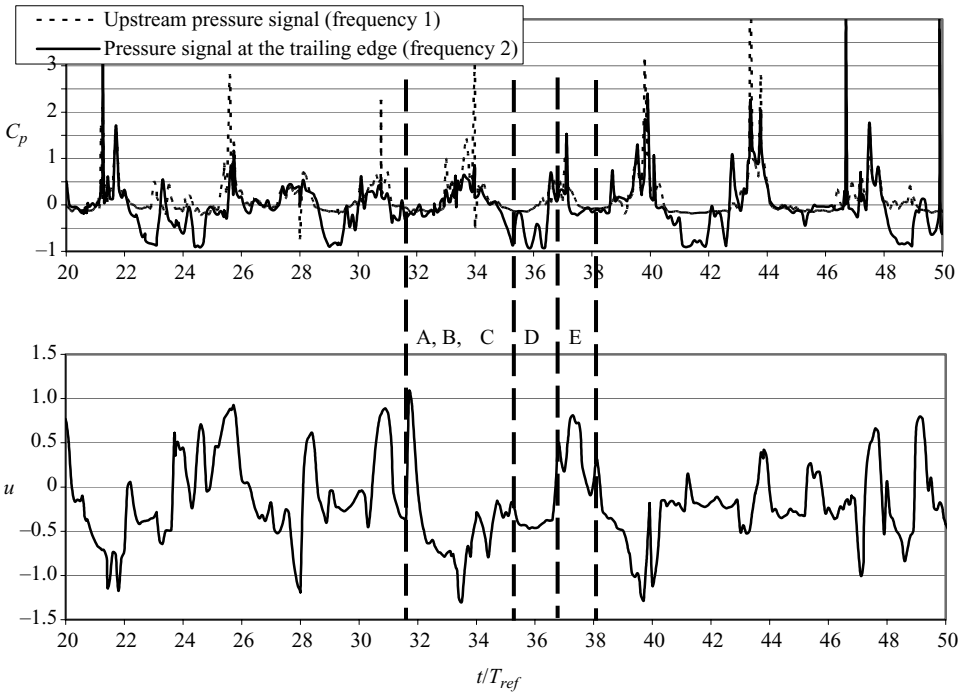

FIGURE 32. Evolution of the pressure and the re-entrant jet during transitional cavity oscillations. ($\sigma = 0.88$, angle of attack 4°7.)

jet is forming. This is delayed until the next oscillation of the pressure-side cavity, so frequency 2 is half frequency 1.

According to the numerical simulations, the modification of the cavitation cycle observed in the case of transitional cavity oscillations is due to the increase of the interaction between the two sides of the foil section, which delays the convection of most of the cloud on the pressure side.

7. Conclusions

Some significant points of the analysis which require further experiments and/or discussion are as follows.

(i) It has been shown that the equations used classically for cavitating flows can be obtained from mass and momentum conservation inside a control volume V, if V is much smaller than the characteristic scale of the flow, and much larger than the size of the liquid/vapour interfaces. These conditions may be a definition for a 'two-phase fluid particle', by analogy with a fluid particle.

(ii) The different models of cavitation are based on similar main assumptions, derived from the diffusion model initially proposed by Ishii. In the present case, the model based on a barotropic state law for the mixture gives results in fair agreement with the experimental ones. However, none of these models takes into account the physics of the mass and momentum transfers between the phases. This would require incorporating some information at the microscopic scale, such as the vaporization rate at the boundary of the vapour bubbles, the slip velocity between liquid and vapour, and also the thermal transfers at the interfaces. Recent direct numerical simulations

performed for example in Caltech by Preston (2003) of the behaviour of a vapour bubble provide some new information concerning these points.

(iii) According to the measurements of the volume fraction of vapour by X-ray absorption, β does not exceed 35 % for small sheet cavities, and 60 % for the large ones. For $L_{cav}/L_{ref} \approx 0.75$, the evolution of the vapour volume inside the cavity $V_v/(L_{cav}U_{ref}^{0.6}\alpha_i^{0.4})$ was plotted as a function of X/L_{cav}, and all results were found very close to a unique curve, for all velocities and all incidence angles. However, other configurations of foil sections, such as NACA geometries, would probably lead to different results.

(iv) The analysis of partial and transitional cavity oscillations has been performed mainly on the basis of the numerical results. Detailed measurement of the instantaneous velocities inside the liquid/vapour medium would enrich the present discussion concerning the different cavitation cycles. These measurements require specific techniques such as endoscopic PIV or X-ray absorption, which are currently being developed by several teams around the world, including the LML laboratory in France.

Concerning the numerical part of this work, the authors would like to express their gratitude to the CNES (French Space Agency) for its continuous support. The numerical model has been developed for fifteen years in the LEGI laboratory (Grenoble, France) with successive contributions of Y. Delannoy and J-L. Reboud, and co-workers.

REFERENCES

Acosta, A. J. 1955 A note on partial cavitation of flat plate hydrofoils. *California Institute of Technology, Rep. E-19.9*.

Arndt, R. E. A., Song, C. C. S, Kjeldsen, M., He, J. & Keller, A. 2000 Instability of partial cavitation: a numerical/experimental approach. *Proc. 23rd Symp. on Naval Hydrodynamics, Office of Naval Research, Val de Reuil, France, National Academic Press, Washington, DC*, pp. 599–615.

Avva, R. K., Singhai, A. K. & Gibson, D. H. 1995 An enthalpy based model of cavitation. *Cavitation and Gas-Liquid Flow in Fluid Machinery Devices*. ASME-FED Vol. 226 (ed. G. Caignaert), pp. 63–70.

de Bernardi, J., Joussellin, F. & Von Kaenel, A. 1993 Experimental analysis of instabilities related to cavitation in turbopump inducer. *Proc. 1st Intl Symp. on Pump Noise and Vibrations*, pp. 91–99.

Callenaere, M., Franc, J.-P., Michel, J.-M. & Riondet, M. 2001 The cavitation instability induced by the development of a re-entrant jet. *J. Fluid Mech.* **444**, 223–256.

Caupin, F. 2005 Liquid-vapour interface, cavitation, and the phase diagram of water. *Phys. Rev.* E **71**, 051605 (1–5).

Ceccio, S. L. & Brennen, C. E. 1992 Dynamics of attached cavities on bodies of revolution. *Trans. ASME: J. Fluids Engng* **114**, 93–99.

Charles, N. 1994 Modélisation d'écoulements cavitants avec effets thermodynamiques. PhD thesis, Institut National Polytechnique de Grenoble, France.

Chen, Y. & Heister, S. D. 1994 A numerical treatment for attached cavitation. *Trans. ASME: J. Fluids Engng* **116**, 613–618.

Chen, Y. & Heister, S. D. 1995 Modeling hydrodynamic non-equilibrium in bubbly and cavitating flows. *Trans. ASME: J. Fluids Engng* **118**, 172–178.

Coutier-Delgosha, O., Fortes-Patella, R. & Reboud, J.-L. 2002 Simulation of unsteady cavitation with a two-equations turbulence model including compressibility effects. *J. Turbulence* **3**, 058, http:\\jot.iop.org.

Coutier-Delgosha, O., Reboud, J.-L. & Delannoy, Y. 2003 Numerical simulations in unsteady cavitating flows. *Intl J. Numer. Meth. Fluids* **42**(5), 527–548.

Coutier-Delgosha, O., Fortes-Patella, R. & Reboud, J.-L. 2003*b* Evaluation of the turbulence model influence on the numerical simulations of unsteady cavitation. *Trans. ASME: J. Fluids Engng* **125**, 38–45.

Coutier-Delgosha, O., Courtot, Y., Joussellin, F. & Reboud, J.-L. 2004 Numerical simulation of the unsteady cavitation behavior of an inducer blade cascade. *AIAA J.* **42** (3), 560–569.

Coutier-Delgosha, O., Devillers, J.-F., Pichon, T. & Leriche, M. 2005 Effect of the wall roughness on unsteady sheet cavitation. *Trans. ASME: J. Fluids Engng* **127**(4), 726–733.

Coutier-Delgosha, O., Devillers, J.-F., Pichon, T., Vabre, A., Woo, R. & Legoupil, S. 2006 Internal structure and dynamics of sheet cavitation. *Phys. Fluids* **18**(1), 017103.

Dang, J. & Kuiper, G. 1998 Re-entrant jet modelling of partial cavity flow on two dimensional hydrofoils. *Trans. ASME: J. Fluids Engng* **121**, 781–787.

Delannoy, Y. 1989 Modélisation d'écoulements instationnaires et cavitants. PhD Thesis, Institut National Polytechnique de Grenoble, France.

Delannoy, Y. & Kueny J.-L. 1990 Two-phase flow approach in unsteady cavitation modelling. *Cavitation and Multiphase Flow Forum.* ASME-FED Vol. 98, pp. 153–158.

Dieval, L., Arnaud, M. & Marcer, R. 1998 Numerical modelling of unsteady cavitating flows by a VOF method. *Proc. 3rd Intl Symp. on Cavitation* (ed. J.-M. Michel & H. Kato), Vol. 2, pp. 243–248.

Drew, D. A. 1983 Mathematical modeling of two-phase flows. *Annu. Rev. Fluid Mech.* **15**, 261–291.

Furness, R. A. & Hutton, S. P. 1975 Experimental and theoretical studies of two-dimensional fixed-type cavities. *Trans. ASME: J. Fluids Engng* **97**, 515–522.

Gopalan, S. & Katz, J. 2000 Flow structure and modeling issues in the closure region of attached cavitation. *Phys. Fluids* **12**, 895–911.

Grogger, H. A. & Alajbegovic, A. 1998 Calculation of the cavitating flow in Venturi geometries using two fluid model. *ASME Paper*, FEDSM99-7364.

Hirschi, R. & Dupont, P. 1998 Partial sheet cavities prediction on a twisted elliptical planform hydrofoil using a fully 3D approach. *Proc. 3rd Intl Symp. on Cavitation* (ed. J.-M. Michel & H. Kato), Vol. 1, pp. 245–249.

Ishii, M. 1975 *Thermo-fluid Dynamic Theory of Two Phase Flow*. Eyrolles, Paris/Scientific and Medical Publications of France, New York.

Jakobsen J. K. 1964 On the mechanism of head breakdown in cavitating inducers. *Trans. ASME: J. Basic Engng*, pp. 291–305.

Joussellin, F., Delannoy, Y., Sauvage-Boutar, E. & Goirand, B. 1991 Experimental investigation on unsteady attached cavities. *Cavitation'91, ASME 1991*, Vol. 116, pp. 61–66.

Kai, H. & Ikehata, M. 1998 Numerical simulation of cavitation on 3D wings and marine propeller by a surface vortex Lattice method. *Proc. 3rd Intl Symp. on Cavitation* (ed. J.-M. Michel & H. Kato), Vol. 2, pp. 281–286.

Kamijo, K., Shimura, T. & Watanabe, M. 1977 An experimental investigation of cavitating inducer instability. *ASME Paper* 77-WA/FW-14.

Kjeldsen, M., Arndt, R. E. A. & Efferts, M. 2000 Spectral characteristics of sheet/cloud cavitation. *Trans. ASME: J. Fluids Engng* **122**, 481–487.

Knapp, R. T., Daily, J. T. & Hammit, F. G. 1970 *Cavitation.* McGraw Hill.

Kubota, A., Kato, H. & Yamaguchi, H. 1992 A new modelling of cavitating flows: a numerical study of unsteady cavitation on a hydrofoil section, *J. Fluid Mech.* **240**, 59–96.

Kunz, R. F., Boger, D. A., Stinebring, D. R., Chyczewski, T. S., Lindau, J. W., Gibeling, H. J., Venkateswaran, S. & Govindan, T. R. 2000 A preconditioned implicit method for two-phase flows with application to cavitation prediction. *Computers Fluids* **29**(8), 849–875.

Laberteaux, K. R. & Ceccio, S. L. 2001 Partial cavity flows. Part 1. Cavities forming on models without spanwise variation. *J. Fluid Mech.* **431**, 1–41.

La porta, A., Voth, G. A., Moisy, F. & Bodenschatz, E. 2000 Using cavitation to measure statistics of low pressure events in large-Reynolds-number turbulence. *Phys. Fluids* **12**(6), 1485–1496.

Le, Q., Franc, J.-P. & Michel, J.-M. 1993 Partial cavities: global behaviour and mean pressure distribution. *J. Fluids Engng* **115**, 243–248.

Leroux, J.-B., Coutier-Delgosha, O. & Astolfi, J.-A. 2005 A joint experimental and numerical analysis of mechanisms associated to unsteady partial cavitation. *Phys. Fluids* **17**(5), 052101.

Lush, P. A & Peters, P. I. 1982 Visualisation of the cavitating flow in a venturi type duct using high-speed cine photography. *Proc. IAHR Conf. on Operating Problems of Pump Stations and Power Plants*, Vol. 5, pp. 1–13.

Matsumoto, Y. 1998 Bubble dynamics in cavitation. *Proc. 3rd Intl Symp. on Cavitation* (ed. J.-M. Michel & H. Kato), Vol. 1, pp. 3–8.

Merkle, C. L., Feng, J. &. Buelow, P. E. O. 1998 Computational modelling of the dynamics of sheet cavitation. *Proc. 3rd Intl Symp. on Cavitation* (ed. J.-M. Michel & H. Kato), Vol. 2, pp. 307–314.

Orszag, S. A. 1993 *Renormalization Group Modelling and Turbulence Simulations, Near Wall Turbulent flows*. Elsevier.

Patankar, S. V. 1981 *Numerical Heat Transfer and Fluid Flow*. Hemisphere.

Pham, T. M., Larrarte, F. & Fruman, D. H. 1999 Investigation of unsteady sheet cavitation and cloud cavitation mechanisms. *J. Fluids Engng* **121**, 289–296.

Preston, A. T. 2003 Modeling heat and mass transfer in bubbly cavitating flows and shock waves in cavitating nozzles. PhD Dissertation, California Institute of Technology.

Reboud, J.-L. & Stutz, B. 1995 Analyse de l'écoulement dans les poches de cavitation : modèle diphasique liquide-vapeur à deux fluides. *Final Report* 95/CNES/3171.

Reboud, J. L., Stutz, B. & Coutier, O. 1998 Two phase flow structure of cavitation: experiment and modeling of unsteady effects. *Proc. 3rd Intl Symp. on Cavitation* (ed. J.-M. Michel & H. Kato), Vol. 2, pp. 203–208.

Sauer, J. & Schnerr, G. H. 2000 Unsteady cavitating flow – A new cavitation model based on modified front capturing method and bubble dynamics. *Proc. Fluids Engineering Summer Conference*. FEDSM2000/11095.

Senocak, I. & Shyy, W. 2004*a* Interfacial dynamics-based modelling of turbulent cavitating flows, Part-1: Model development and steady-state computations. *Intl J. Numer. Meth. Fluids* **44**(9), 975–995.

Senocak, I. & Shyy, W. 2004*b* Interfacial dynamics-based modelling of turbulent cavitating flows, Part-2: Time-dependent computations. *Intl J. Numer. Meth. Fluids* **44**(9), 997–1016.

Shin, B. R. & Ikohagi, T. 1998 A numerical study of unsteady cavitating flows. *Proc. 3rd Intl Symp. on Cavitation* (ed. J.-M. Michel & H. Kato), Vol. 2, pp. 301–306.

Singhal, A. K., Athavale, M. M., Li, H.-Y. & Jiang, Y. 2002 Mathematical basis and validation of the full cavitation model. *J. Fluids Engng* **124**(3), 617–624.

Song, C. C. S. & He, J. 1998 Numerical simulation of cavitating flows by single-phase flow approach. *Proc. 3rd Intl Symp. on Cavitation* (ed. J.-M. Michel & H. Kato), Vol. 2, pp. 295–300.

Stutz, B. & Legoupil, S. 2003 X-ray Measurements within unsteady cavitation. *Exps. Fluids* **35**(2), 130–138.

Stutz, B. & Reboud, J.-L. 1997*a* Experiments on unsteady cavitation. *Exps. Fluids* **22**, 191–198.

Stutz, B. & Reboud, J.-L. 1997*b* Two-phase flow structure of sheet cavitation. *Phys. Fluids* **9**(12), 3678–3686.

Stutz, B. & Reboud, J.-L. 2000 Measurements within unsteady cavitation. *Exps. Fluids* **29**, 545–552.

Thai Van, D., Minier, J. P., Simonin, O., Freydier, P. & Olive, J. 1994 Multidimensional two-fluid model computation of turbulent dispersed two-phase flows. *Numerical Methods in Multiphase Flows*. ASME-FED Vol. 185, pp. 277–291.

Tsujimoto, Y., Kamijo, K. & Yoshida, Y. 1993 A theoretical analysis of rotating cavitation inducers". *J. Fluids Engng* **115**, 135–141.

Ventikos, Y. & Tzabiras, G. 1995 A numerical study of steady and unsteady cavitation phenomenon around hydrofoils. *Proc. CAV'95 Intl Symp. on Cavitation*, pp. 441–448.

Watanabe, S., Tsujimoto, Y. & Furukawa, A. 2001 Theoretical analysis of transitional and partial cavity instabilities. *J. Fluids Engng* **123**, 692–697.

Wei, Y. S. & Sadus, R. J. 2000 Equations of state for the calculation of fluid-phase equilibria. *AIChE J.* **46**(1), 169–196.

Wilcox, D. 1998 *Turbulence Modeling for CFD*. DCW Industries, Inc., La Canada, California, USA.

Wu, J., Wang, G. & Shyy, W. 2005 Time-dependent turbulent cavitating flow computations with interfacial transport and filter based models. *Intl J. Numer. Meth. Fluids* **49**(7), 739–761.

Yu, P.-W., Ceccio, S. & Tryggvason, G. 1995 The collapse of a cavitation bubble in shear flows – A numerical study. *Phys. Fluids* **7**(11), 2608–2616.

Yuan, W. & Schnerr, G. H. 2003 Numerical simulation of two-phase flow in injection nozzles: interaction of cavitation and external jet formation. *J. Fluids Engng* **125**, 963–969.

Zhu, J. 1991 A low diffusive and oscillation-free convection scheme. *Commun. Appl. Numer. Meth.* **7**, 225–232.